

Public document

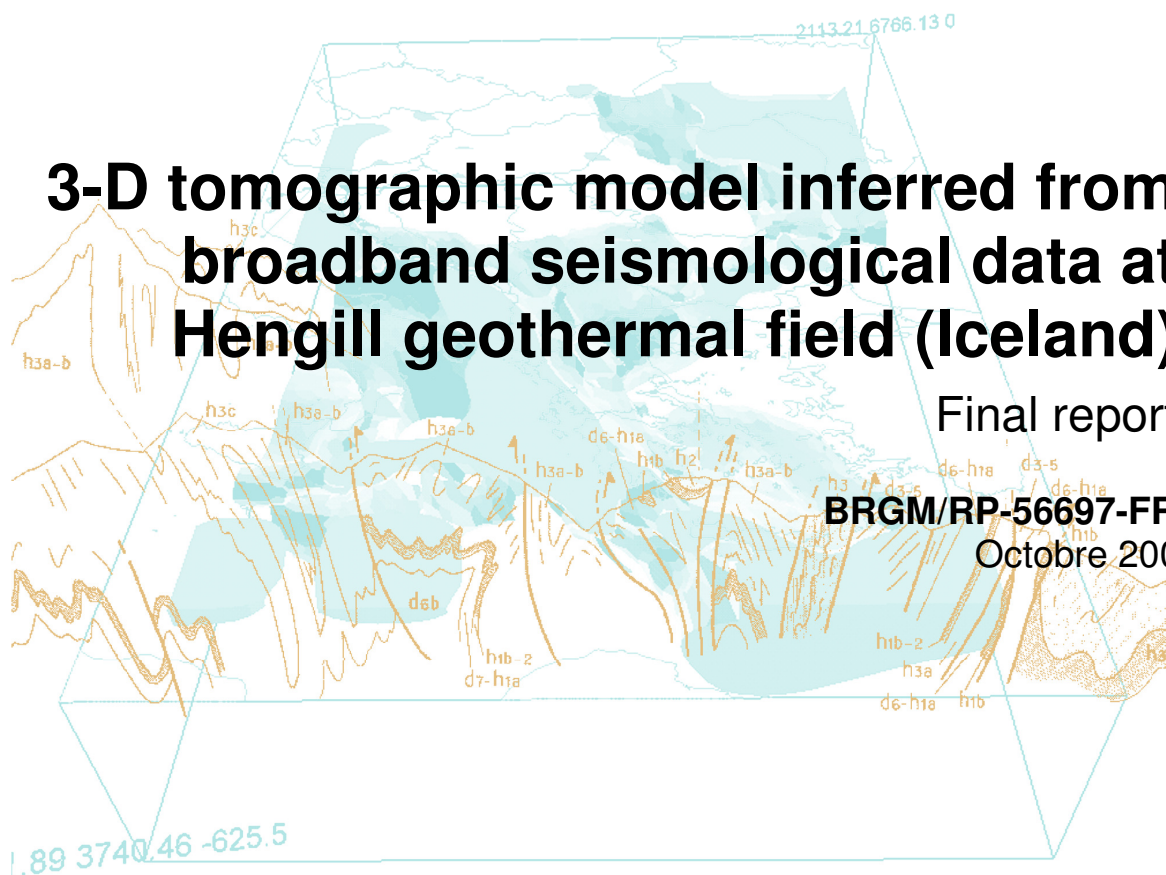


3-D tomographic model inferred from broadband seismological data at Hengill geothermal field (Iceland)

Final report

BRGM/RP-56697-FR

Octobre 2008



3-D tomographic model inferred from broadband seismological data at Hengill geothermal field (Iceland)

Final report

BRGM/RP-56697-FR

Octobre 2008

Study carried out as part of
Research activities within the framework of the Enhanced
Geothermal Innovative Network for Europe (ENGINE) European
Project, n° 518378 - BRGM 2008

Philippe Jousset

With the collaboration of
Didier Bertil, Xavier Serey

Checked by:

Name: H. Fabriol

Date:

Signature:

(or Original signed by:)

Approved by:

Name: H. Modaresi

Date:

Signature:

(or Original signed by:)

BRGM's quality management system is certified ISO 9001:2000 by AFAQ

Keywords: broadband seismology, 3-D tomography, high enthalpy, geothermal energy, Iceland, Hengill

In bibliography, this report should be cited as follows: Philippe Jousset, 2007. 3-D tomographic model from broadband seismological data at Hengill geothermal field (Iceland), Final report, BRGM/RP-56697-FR, p, ill.

© BRGM, 2008. No part of this document may be reproduced without the prior permission of BRGM.

Synopsis

Hengill volcanic complex is located at a triple-junction between two segments of the spreading ridge between North American plate and European plate, and a transform fault (South Iceland Seismic Zone). A well developed geothermal system is exploited and the extracted vapour allows Icelanders to sustain for part of their needs in power supply and heat. This area is subject to intense seismic activity, which is monitored continuously by a permanent seismological network, the SIL network of the Icelandic Meteorological Office. The recorded seismic activity has been related to the cooling of deep magmatic bodies and to geothermal fluids activity within Hengill volcanic complex.

In order to improve our understanding of the relationships between seismic activity and vapour production, a network including 7 broadband seismological stations was setup from June 26th, 2006 till October 17th, 2006, on the geothermal system of Hengill (Jousset and François, 2006), in the framework of the FP6 funded I-GET project.

This report describes the processing carried out to retrieve data from the disks and describes algorithms used in order to extract significant information from data about the seismic activity at the Hengill geothermal field and the neighbouring volcanic complex. The data set consists of broadband seismological data from the IGET network and from 3 stations of the SIL network, allowing us a more accurate analysis of the seismic activity within the area. We performed

- detection and classification of recorded seismicity
- improvement of hypocenter locations and structural features of the geothermal system by tomography techniques

An interactive matlab interface, Seismotool (Jousset, 2006), was used and improved to process the seismic data set. Data analysis allowed us to detect more than 600 earthquakes, amongst which long-period earthquakes were observed (Jousset et al., 2006).

The accurate location of the earthquakes and the knowledge of the velocity structure is improved by performing the joint inversion of microseismicity hypocenters and 3D velocity model (Haberland et al., 2006). We used 339 micro-earthquakes with clear P- and S- arrival times to image the compression P-wave and shear S-wave structure of the geothermal reservoir applying tomography inversion to the 2266 P- and 2432 S-waves arrival times with the computer program SIMULPS12 (Evans et al., 1994), which solves simultaneously for earthquake locations and crustal structure by the iterative damped-least-square method. The program VELEST (Kissling, 1994) provides one-dimensional v_P (and v_S) models used as a starting point for the inversion. A careful choice on the earthquakes and inversion parameters has been done prior to the inversion (Eberhart-Phillips, 1993).

By doing so, we show that

- Results from the simultaneous inversion for the 3-D velocity structure and the hypocenter determination is able to give us more insights than previously obtained, especially on the existence of a high velocity anomaly in the area of OKelduhals from about 2 to 4 km depth and a low v_p/v_s ratio anomaly beneath the northern part of Mt. Hengill below 4-5 km. This anomaly has been detected previously and was related to the possible presence of supercritical fluids (Tryggvason, 2002). Our work gives more details on the extension of this anomaly, but its northern and western limit cannot be determined accurately by lack of coverage of the network in those areas.
- These detailed structural features at Hengill suggest new opportunities for studying the relation between local seismicity and fluid exploitation.

Contents

1. Introduction	9
2. The geothermal field at Hengill within the tripple junction tectonic setting	11
2.1. GEOLOGICAL SETTING OF HENGILL VOLCANO COMPLEX	11
2.2. SEISMICITY AT HENGILL VOLCANO	12
3. Broadband data acquisition and processing	15
3.1. THE SEISMIC ICELANDIC LOWLAND NETWORK.....	15
3.2. IGET DATA PROCESSING.....	16
3.2.1. Network, data availability and format.....	16
3.2.2. Seismotool interactive tool.....	18
3.3. SIGNAL DETECTION, CLASSIFICATION AND CATALOGUES.....	19
3.4. P- AND S- ARRIVAL TIMES PICKING METHOD.....	22
3.5. PHASES STATISTICS	23
4. Joint inversion of hypocenter location and 3-D velocity model for Hengill area	25

4.1. PREVIOUS STUDIES AND METHODOLOGY	25
4.2. METHODOLOGY	25
4.3. V_p/V_s RATIO FROM WADATI DIAGRAM ANALYSIS	26
4.4. JOINT HYPOCENTER LOCATION AND 3-D MODEL TOMOGRAPHY INVERSION.....	27
4.4.1. <i>a priori</i> hypocenter location for inversion and methodology	27
4.4.2. VELEST 1-D inversion.....	29
4.4.3. 3-D inversion using SIMULPS12	38
5. Results and discussion.....	47
5.1. DISTRIBUTION OF EARTHQUAKES.....	47
5.2. VELOCITY STRUCTURE	48
5.3. STRUCTURE OF HENGILL GEOTHERMAL SYSTEM	49
6. References	51

List of illustrations

Figure 1 – SIL network in Iceland. IGET broadband network at Hengill volcanic complex is located in the South West of Iceland, between the 4 stations SAN, BJA, KRO and HEI.....	15
Figure 2 – Gutenberg-Richter law [$\log(N)=a-b*M$] from the 120 earthquakes at Hengill geothermal system of the SIL network catalogue between 25 June 2006 and 30 September 2006. b-value is 0.95.....	16
Figure 3 – Location of the stations used for our study – Note that the SIL station BJA did not record data and was not used.	18
Figure 4 – Principe of the detection of earthquake using the STA-LTA algorithm.....	20

Figure 5 – Earthquake types recorded at Hengill geothermal system at station HE7. (Left) seismograms; (middle) amplitude spectra; (right) spectrogram.	21
Figure 6 – Cumulative high-frequency VT seismicity at Hengill volcano recorded by IGET network from June till October 2006.	22
Figure 7 – Akaike Information criteria semi-automatic picking method.	23
Figure 8 – Statistics on the (left) P and (right) S picks. About 4800 picks were performed, with 80% and 65% being below 0.05 s for P and S waves, respectively.	24
Figure 9 – Wadati diagram on 339 earthquakes of IGET network at Hengill.	27
Figure 10 – Hypocenter locations of the 339 earthquakes obtained by the grid search inversion of the P-wave travel times assuming an homogeneous medium with $v_p=5000$ m/s.	29
Figure 11 – (top) Inverted 1-D P-wave velocity v_p 30 models with lower RMS and (bottom) 339 earthquake hypocenter locations using P-wave arrival times only. The a priori location is below HE3 station at 4 km depth. Left: inverted; best model (lowest RMS) in red. Triangles: IGET network and SIL stations locations.	31
Figure 12 - (top) Inverted 1-D P-wave velocity v_p 30 models with lower RMS and (bottom) 339 earthquake hypocenter locations using P- and S-waves arrival times. The a priori location is below HE3 station at 4 km depth. Left: inverted; best model (lowest RMS) in red. Triangles: IGET network and SIL stations locations.	32
Figure 13 - Inverted 1-D v_p models using fixed hypocenter location (339 earthquakes). A priori hypocenter location at lat=64.0N; lon=21.5W - depth 4 km.	33
Figure 14 – Inverted 1-D v_p models using fixed hypocenter location (339 earthquakes). a priori hypocenter location outside network aperture at lat=64.1N; lon=21.4W - depth 4 km. Compare with Figure 11 bottom results with HE3 a priori location.	34
Figure 15 - Inverted 1-D v_p models using a priori locations from the preliminary inversion using P-arrival times only.	35
Figure 16 - Inverted 1-D v_p models using a priori locations from the preliminary inversion (top) using P- and S- arrival times. This model is the one used for further inversions.	36
Figure 17 – Trade-off curve of the damping between the data variance and model variance for the case of 3-D v_p inversion sampled every 2 km. The damping parameter value chosen in this case will be 2.	39
Figure 18 – Horizontal slices of P-wave velocity 3-D tomography inversion at Hengill using a grid of 2 km. Triangles represent station locations. Continuous lines indicate constant velocity. White circles represent earthquake location within a -0.5/+0.5 km range from the slice depth.	40
Figure 19 - Horizontal slices of P-wave velocity 3-D tomography inversion at Hengill using a grid of 1 km. Triangles represent station locations. Continuous lines indicate constant velocity. White circles represent earthquake location within a -0.5/+0.5 km range from the slice depth.	40
Figure 20 – E-W cross-sections of (top) P-wave velocity at Hengill geothermal system from the 3-D tomography inversion with a grid of 2 km. Continuous lines indicate constant velocity. (bottom) spread values of the tomography. Dark shading (low spread values) in the center of the model volume indicate a good resolution. The outer regions show a reduced resolution as indicated by lighter shading. Triangles represent station	

locations at the surface indicated by a thick black line. White circles represent earthquake location within a $-0.05/+0.05$ degree range from the position of the cross-section..... 41

Figure 21 – N-S cross-sections of (top) P-wave velocity at Hengill geothermal system from the 3-D tomography inversion with a grid of 2 km. Continuous lines indicate constant velocity. (bottom) spread values of the tomography. Dark shading (low spread values) in the center of the model volume indicate a good resolution. The outer regions show a reduced resolution as indicated by lighter shading. Triangles represent station locations at the surface indicated by a thick black line. White circles represent earthquake location within a $-0.05/+0.05$ degree range from the position of the cross-section..... 42

Figure 22 - E-W cross-sections of (top) P-wave velocity 3-D tomography inversion at Hengill using a grid of 1 km. Black triangles represent station locations at the surface indicated by a thick black line. Continuous lines indicate constant velocity. (bottom) spread values of the tomography. Dark shading (low spread values) in the center of the model volume indicate a good resolution. The outer regions show a reduced resolution as indicated by lighter shading. White circles represent earthquake location within a $-0.05/+0.05$ degree range from the position of the cross-section. 43

Figure 23 - E-W cross-sections of (top) P-wave velocity 3-D tomography inversion at Hengill using a grid of 1 km. Black triangles represent station locations at the surface indicated by a thick black line. Continuous lines indicate constant velocity. (bottom) spread values of the tomography. Dark shading (low spread values) in the center of the model volume indicate a good resolution. The outer regions show a reduced resolution as indicated by lighter shading. White circles represent earthquake location within a $-0.05/+0.05$ degree range from the position of the cross-section. 44

Figure 24 – Comparison between the resistivity model obtained from the inversion of TEM and magnetotelluric data (Arnasson et al., 2008) and the P-wave velocity model obtained from the tomography of broadband observations at Hengill geothermal system at different depths (left,top: 1800m; right, top: 2400 m; left, bottom: 3100 m; right, bottom: 3900 m)..... 50

1. Introduction

Hydrothermal systems offer a low CO₂ emission long-term alternative as energy supply (Barnea, 1972). The exploitation of geothermal energy is limited at present, because drilling exploration wells is expensive, and hydrothermal systems are often associated with volcanic and seismic activity, which may put geothermal exploitation at risk (Ward, 1972).

In order to reduce the risk of dry-drilling, the structural features of the targeted geothermal system is a critical knowledge prior to drilling. Amongst the geophysical methods to infer the crustal structure, passive seismology is of first choice. Both classical local seismic tomography in those areas where local seismicity is numerous (e.g., Benz et al., 1996), and newly developed surface wave tomography techniques applied to ambient noise have been shown able to image detailed crustal subsurface structure (Brenquier et al., 2007).

Recent development of broadband seismometers allows the acquisition of broadband signals, like long period earthquakes (0.5 s to 5 s) and tremor and very long period earthquakes (above 5 s), having specific characteristics described mainly in terms of duration and frequency content. These signals have been observed at many active volcanoes (e.g., Neuberg et al., 1994), hydrothermal systems (and even oil fields (Dangel et al., 2003)). We applied these techniques to a data set from a temporary broadband seismological network of 7 broadband seismic stations set up at Hengill volcano area, Iceland. The two main objectives are:

- To record passive seismicity associated with the Hengill volcanic complex, in relation with the exploitation of the geothermal system, especially within the long-period frequency band (< 5 Hz) and relate the seismicity to the known structural features of the geothermal system.
- To improve our knowledge of the 3-D structure of the exploited geothermal system, by using local seismic tomography inversion techniques, with micro-earthquakes recorded by the network. Previous tomography studies reveal the main structural features of the volcanic area and the triple junction, but they are not sufficiently detailed for a detailed analysis of the structural features of the geothermal system itself. In particular, the v_P/v_S ratio and attenuation measurements are very diagnostic of pore-fluid and temperature conditions when used in conjunction with v_P (Evans et al., 1994), in relation with the non-double couple earthquakes and LP earthquakes (Jousset & Chouet, 2008). The improvement of the velocity model is required in order to locate possible long-period earthquakes (e.g., Lokmer et al., 2007).
- To analyse the frequency content of the seismicity, especially the non-double couple events (Miller et al., 1998), thought to be possible signatures of fluids

movements linked to the exploitation and relate them to long-period earthquakes (Chouet, 1996; Jousset & Chouet 2008).

In the present study, we focus on the improvement of the resolution of the structural feature of the geothermal field. After we give elements on the geological settings (Section 2), we describe the data acquisition and processing in Section 3. We explain then our strategy to perform the tomography inversions (Section 4); finally we discuss the results. The theory and method of local tomography inversion has been described in detail by a number of authors, e.g., Thurber (1983), Thurber (1986), Kissling (1988), Ellworth (1991), Eberhart-Phillips (1986), Eberhart-Phillips (1993), Iyer & Hirahara (1993), Kissling (1994), Thurber (1993), Eberhart-Phillips (1994), and recently in Tryggvason (2002), Kulakov et al. (2007).

2. The geothermal field at Hengill within the triple junction tectonic setting

2.1. GEOLOGICAL SETTING OF HENGILL VOLCANO COMPLEX

Hengill Triple Junction system was found in the late sixties to have high potential for vapour and geothermal energy production centres Gunnarsson et al., (1992). The geothermal activity of the three volcanic systems is expressed in numerous hot springs and fumaroles that occur widespread in the area around the central volcanoes, covering an area of 70 km² (Saemundsson, 1995). The natural heat loss is about 350 MW.

An estimate of the order of magnitude of the total recoverable heat resources in the Hengill area based on the reservoir model (Bödvarsson, 1961), indicated a total of the order of 10¹⁰ tons of water at 220 to 230°C could be produced for about 100 years. The Nesjavelir geothermal power plant is one of the first power plant set up to produce geothermal power in 1986 after extensive exploration studies (Gunnarsson et al., 1992). Over 20 wells up to 2.5 km deep have been drilled for steam and hot water for electricity generation and space heating in Reykjavik. The geothermal activity of Hromundartindur is most intense in the South of the edifice at Ölkelduhàls.

The existence of a large geothermal anomaly at Hengill volcanic systems comes from its specific location within the geodynamical context of Iceland. Hengill volcanic systems are located at the crossing of three tectonic systems:

- (1) the Reykjanes Peninsula, which is the aerial expression of the Reykjanes Ridge spreading between North America plate and Europe plate to the South;
- (2) West Volcanic Zone, spreading between two former plates to the North;
- (3) South Island Seismic Zone - transform zone to the EVZ to the East.

This makes this area a triple junction, ideal for the rising of magma and heat pulses from depth (Foulger, 1995). An intense fissure swarms crosses Mount Hengill and extends from the coast south to Hengill and to north of Lake Thingvallavatn. At the Eastern edge of Hengill volcanic system, there is another separate volcanic production system called Hromundartindur. A third volcanic system is the Grensdalur volcano.

Even if knowing the precise location of the highest geothermal potential is not very critical in this area (90 % of wells are productive when drilled!, Arnasson, pers. comm.), Hengill geothermal system structure is one of the best studied using local seismicity (Foulger, 1995; Miller et al., 1998), and may be seen therefore as a natural

laboratory to study new exploration techniques, like broadband seismology, and improve our knowledge about Hengill geothermal system as well, as questions remain unsolved (Tryggvason et al., 2002).

The Hengill (Iceland) geothermal system, where the exploration targets, is mainly located in volcanic centres (down to 2000 m depth), within a rift zone characterised by both porous and fissure oriented anisotropic permeability. At present, geothermal fluids are mined at the depth of about 2 km, but the ongoing Iceland Deep Drilling Project (IDDP) aims at extracting supercritical fluids from the depth of about 4 km.

2.2. SEISMICITY AT HENGILL VOLCANO

Cooling, mostly due to natural heat loss, and consequential thermal contraction and cracking in the heat source, are thought to be responsible for the continuous small-magnitude earthquake activity in this area (Miller et al., 1998). This mode of earthquake induction was suggested following the observation that many of the earthquakes have merely non-double-couple focal mechanisms¹ with large explosive components (Foulger & Long, 1984). The mechanism responsible for those non-double-couple may be fluid flow into newly formed cracks (Miller et al., 1998; Sens-Schönfelder, 2006).

Many studies at volcanoes points to the role of fluids in the crust to explain characteristics of seismic signatures at volcanoes and hydrothermal systems. The activity of hydrothermal systems involves various physical and chemical mechanisms, like fluid migration, rock/fluid interaction, ... Coupled and simultaneous observations of seismic activity, electric currents, gravity changes, deformation, chemical fluid composition,... allow a better knowledge of parameters and their coupling within complex mechanisms. This multi-parameter global approach, which encloses the whole hydrothermal system, helps us to discriminate critical parameters for efficient monitoring.

Recently developed broadband seismometers (Usher, 1979) allow the acquisition of long-period (LP) signals (0.1 to 2 s) and very-long-period (VLP) signals (2 to 100 s). Broadband seismology allows us to describe and quantify fundamental geometrical and dynamical parameters within hydrothermal systems (Chouet, 1996). Detailed analysis of temporal and frequency characteristics (e.g., Neuberg et al., 1994; Jousset et al., 2003) and waveform inversion of LP earthquakes (e.g., Chouet 2006; Jousset & Chouet, 2008) allowed many studies to describe and quantify fundamental parameters within hydrothermal systems, like geometrical and dynamical interaction between fluids and solid. These studies and research programs proved that this technique was determinant to understand seismic signals issued from hydrothermal systems associated to volcanoes (Kumagai et al., 2002), but also at oil fields (Dangel, 2003).

¹ Tectonic earthquakes have generally double couple mechanism, as they correspond to strike-slip only. When fluids are involved, tensile components and explosive components of the moment tensor are involved, which are representative of non-double-couple mechanisms.

On geothermal systems, such a technique is new and was initially applied at Bouillante, Guadeloupe, French Antilles (Jousset et al., 2004; Jousset, 2006). With the use of appropriate techniques to analyse such seismicity (Legrand et al., 2000), it is possible to find better locations of fracture (Jousset & Chouet, 2008), and therefore potentially to reduce the risk of dry-drilling.

3. Broadband data acquisition and processing

3.1. THE SEISMIC ICELANDIC LOWLAND NETWORK

The Iceland Meteorological Office is in charge of monitoring the seismicity in Iceland. The Seismic Iceland Lowland (SIL) network (Stefansson et al., 1993; Jacobsdottir, 2008) comprises at present a large number of stations (Figure 1).

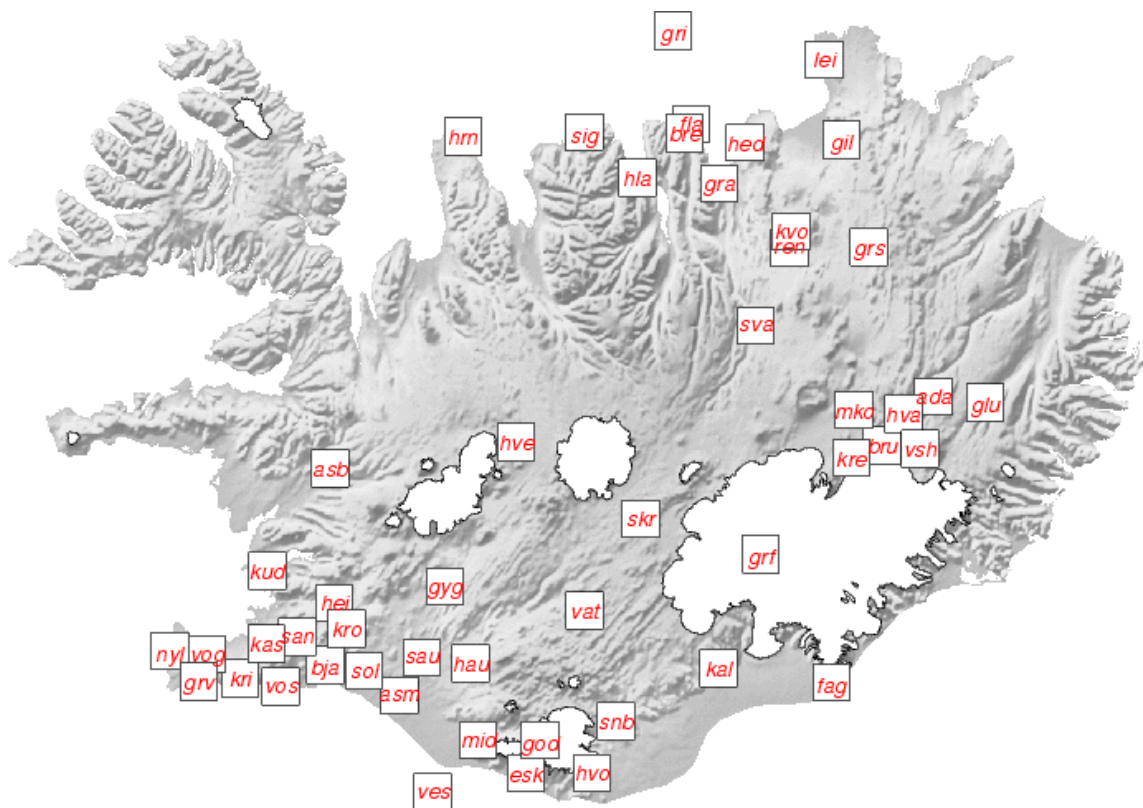


Figure 1 – SIL network in Iceland. IGET broadband network at Hengill volcanic complex is located in the South West of Iceland, between the 4 stations SAN, BJA, KRO and HEI.

This network records and processes seismic data in Iceland in real time, giving on the web a catalogue of localised earthquakes updated regularly. It is possible to retrieve the catalogue from any period of time. The IGET broadband network was setup from the 19th of June till the 20th of October 2006. From the retrieved 3266 events in this period in the complete data base (minimum latitude=52 N; maximum latitude=80 N; minimum longitude=-35 W; maximum longitude=-10 N), we extracted 154 events localized in the Hengill area (longitude=[-21 27 7.0; -21 06 8.0] and latitude=[63 59 57;

64 8 1.6], which should have been recorded by IGET network. This number of event is a minimum, as there may well be that smaller earthquakes not localized by the SIL network may have been recorded by IGET broadband network.

SIL catalogue analysis

The analysis of the b-value using SIL data leads to a value of 0.95, in accordance with the observed value at Hengill over yearly analysis (Agustsson and Halldorsson, 2005). This value is in the range of values observed at other geothermal area (e.g., Henderson et al., 1999; Riedel et al, 2003).

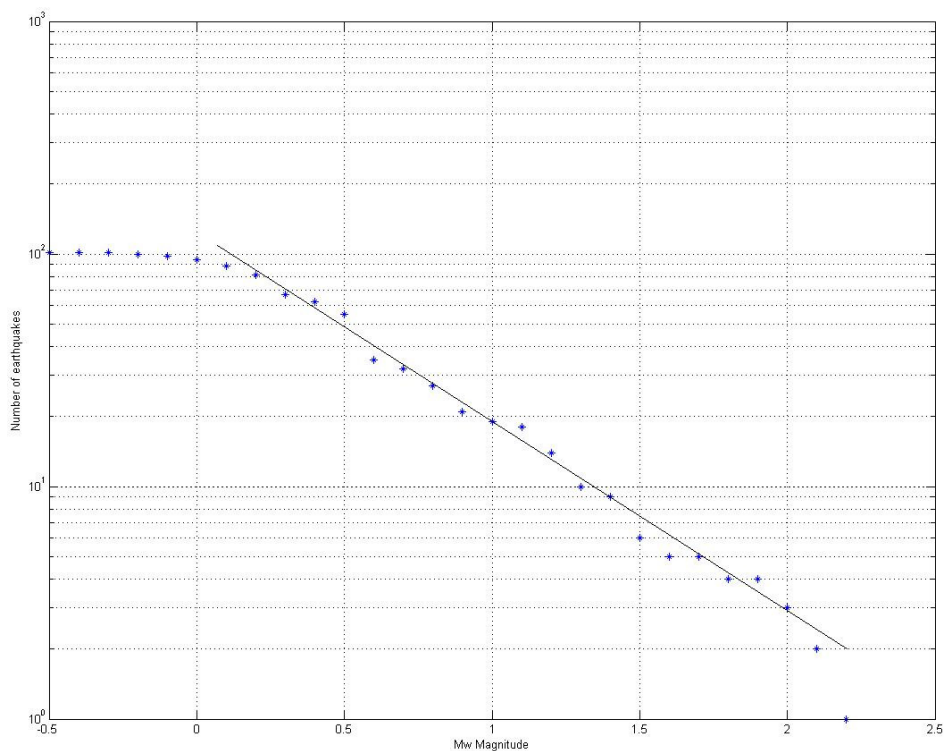


*Figure 2 – Gutenberg-Richter law [$\log(N)=a-b*M$] from the 120 earthquakes at Hengill geothermal system of the SIL network catalogue between 25 June 2006 and 30 September 2006. b-value is 0.95.*

3.2. IGET DATA PROCESSING

3.2.1. Network, data availability and format

Three sources of data were used. We installed 2 types of instruments and data loggers, and we used 3 stations of the SIL network (Jakobsdottir, 2008):

* 5 Güralp CMG-ESP broadband seismometers (frequency 0.0083 Hz to 50 Hz) and SAM data logger: files are stored in a hard disk requesting the use of a specific procedure to retrieve usable seismic data.

* 2 Güralp CMG-40T broadband seismometers (frequency 0.0167 Hz to 50 Hz) and DCM data logger in which usable seismic data are directly available.

* 3 Lennartz stations belonging to the SIL network (Stefanson et al., 1993) managed by the Icelandic Meteorological Office.

The detailed description of the network installation is given in Jousset & Francois (2006). Table 1 gives the main characteristics of the stations.

station	Sensor	Frequency band (Hz)	Latitude WGS84	Longitude	Elevation (m)
HE1 (Innstidalur)	CMG-ESP	0.0083-50	64° 04	21° 20	473
HE2 (Hveragerdi)	CMG-ESP	0.0083-50	64° 01	21° 13	93
HE3 (Ölkelduhals)	CMG-ESP	0.0083-50	64° 03	21° 15	390
HE4 (Hengillshalsà)	CMG40T	0.0167-50	64° 02	21° 18	375
HE5 (Sporhelldalur)	CMG-ESP	0.0083-50	64° 07	21° 17	373
HE6 (Kyllisfell)	CMG-ESP	0.0083-50	64° 04	21° 11	360
HE7 (Krossjöll)	CMG40T	0.0167-50	64° 05	21° 14	320
HEI (Heidarbaer)	Lennartz 5s	0.2-50	64° 12	21° 14	162
KRO (Krokur)	Lennartz 5s	0.2-50	64° 06	21° 07	147
SAN	Lennartz 5s	0.2-50	64° 03	21° 34	208

Table 1 –Seismological network used in this study

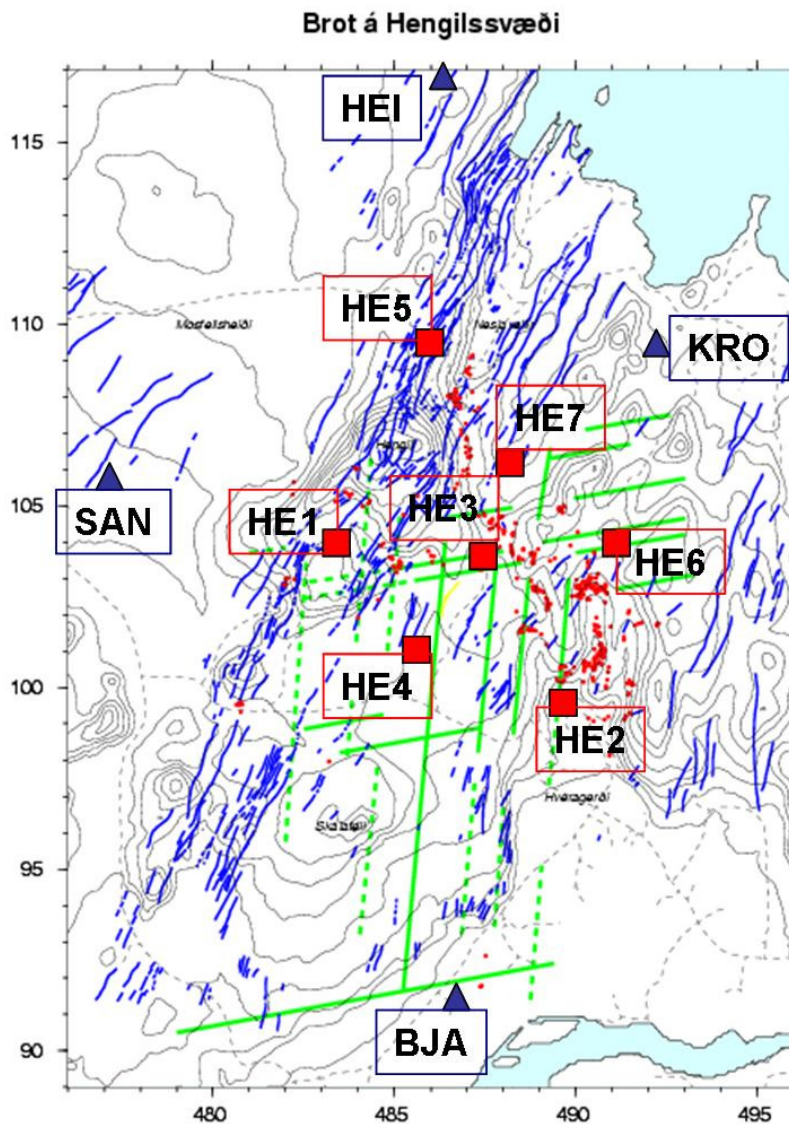


Figure 3 – Location of the stations used for our study – Note that the SIL station BJA did not record data and was not used.

3.2.2. Seismotool interactive tool

Our data set comprises therefore three sorts of files that had to be arranged in a common format for consistent processing. All the tasks required to read, process and classify seismic data for the networks have been performed using an integrated tool written in Matlab for network local seismicity analysis and processing, called Seismotool (Jousset, 2006). It is an interactive platform in which automatic detection

and processing is applied to the 4 months data set using sliding windows, as if data would be acquired in real-time. To do so, Seismotool performs several tasks automatically:

- Reads data files according to the file format at all stations for a duration of 3 hours
- Performs the detection of events using a STA/LTA technique of the envelope of the signals
- Performs the calibration of events according to the instrumental response provided by the constructor and stored in a database
- Classify events according to the number of stations at which the detection flag was raised and constitutes catalogue.

In the following, details on each of those procedures are given.

3.3. SIGNAL DETECTION, CLASSIFICATION AND CATALOGUES

In order to detect events, we performed a Hilbert transform on each of the 3 components of the continuous data, and we computed the ratio between the STA (Short Term Average, 0.5 s) and LTA (Long Term Average, 10 s) of the velocity amplitude at each station. An event is detected when the STA/LTA ratio exceeds a threshold (fixed at 2 for our data set), for the three components at the same time. If the threshold is too low, many events are detected, but may likely correspond to higher noise level; if the threshold is too high, low magnitude earthquakes may be missed, and the final data set is incomplete (Figure 4). If an event is detected at several stations of the network within a period of time compatible with the size of our network and reasonable average wave velocities within Hengill geothermal system, then one minute length data record (15 seconds before the trigger and 45 seconds after the trigger) is extracted for all stations for this event for further analysis.

By continuously tracking both the location of the stations and the number of stations that triggered the STA/LTA algorithm, we are able to give a first rough classification: large and close earthquakes will be recorded at all the stations, whereas small and localised earthquakes are recorded only at some of the station of the network. When an event is detected to at least 3 stations of the network, the waveform of the signal is extracted from the continuous data sorted and recorded into a directory according to the number of stations of the network that detected the event (data from all stations are extracted).

Once event detection and automatic classification has been performed, a visual analysis of each waveform at each station is performed in order to read as much as information as possible from the data. This task consists in recording all valuable information seen in the waveforms that allows us to discriminate the waveform and identify the nature of the signal (noise, local earthquake, teleseism, long-period event, ...), to locate earthquakes (P- and S- wave arrival times), to quantify the magnitude of

the earthquakes, to quantify anisotropy in the area, ...These tasks have been automatized in Seismotool. For each classified earthquake type, a list of attributes is recorded, that Seismotool is able to read again later for further analysis.

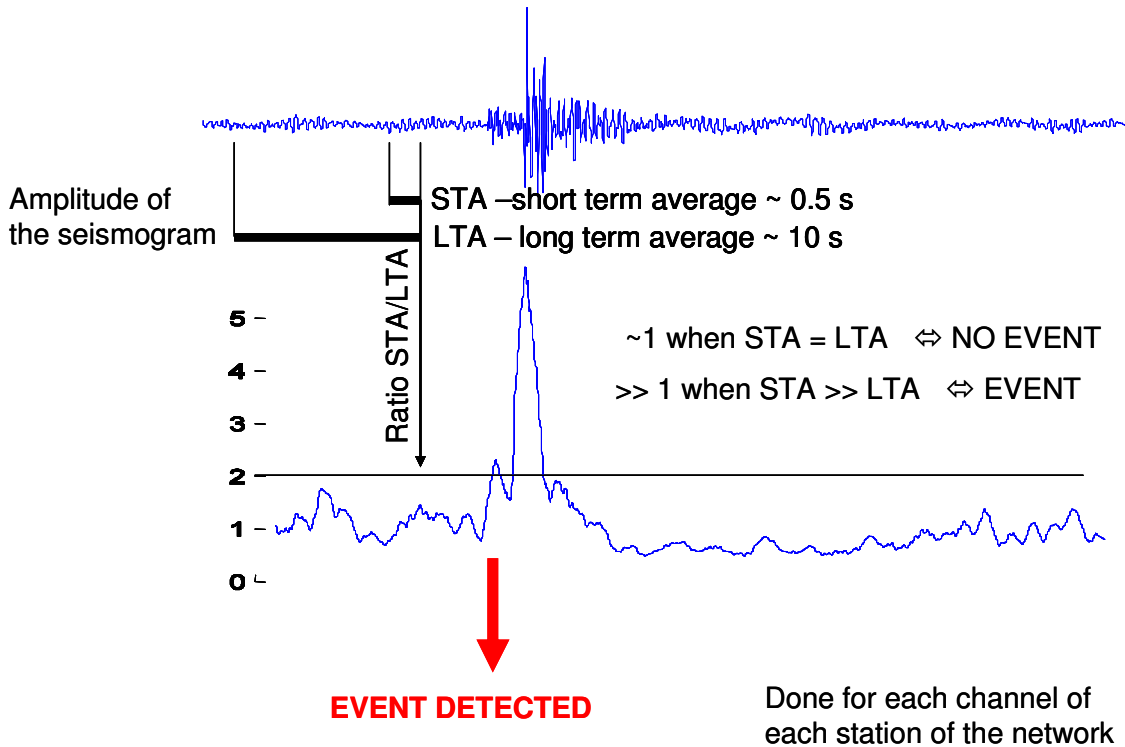


Figure 4 – Principe of the detection of earthquake using the STA-LTA algorithm.

	SIL network	Hengill earthquakes	Tectonic earthquakes	Long-period earthquakes
June 2006 (end)	5	24	13	1
July 2006	43	202	48	8
August 2006	36	149	20	4
Sept. 2006	36	49	18	6
Total	120	424	99	19

Table 2 – Summary of the IGET Hengill earthquake catalogue between 25th June and 20th October, 2006.

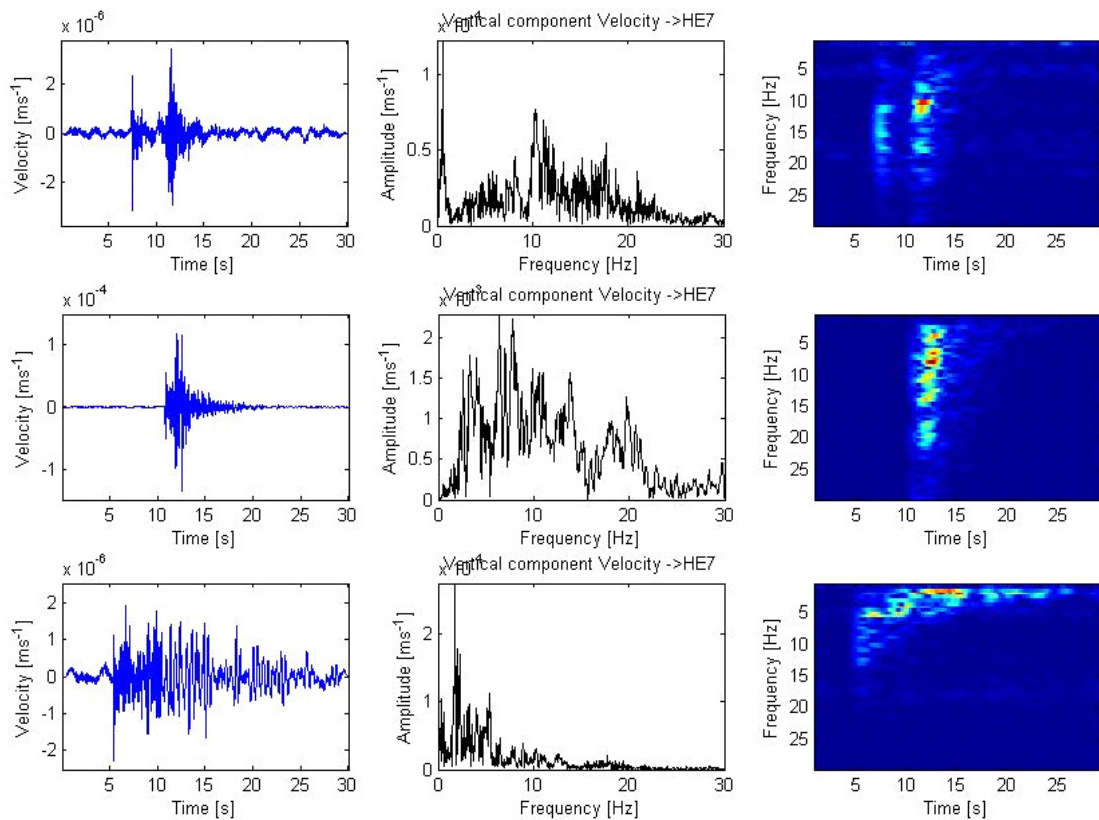


Figure 5 – Earthquake types recorded at Hengill geothermal system at station HE7. (Left) seismograms; (middle) amplitude spectra; (right) spectrogram.

This technique allowed us to detect more than 600 events from the 20th of June 2006 till the 19th of October 2006 and classify them (Figure 5, Table 2). 500 micro-earthquakes (volcano-tectonics) located within the Hengill area, 40 tectonic earthquakes originating from outside Hengill volcano and 30 events called 'long-period event'. Note that the SIL network recorded 130 locatable earthquakes for the same period of time, all detected by our detection algorithm. We conclude that our detection procedure was effective to catch smaller seismicity within Hengill volcano.

Many events are not reported in SIL and USGS catalogues, which shows that our denser network was properly designed to record micro-seismicity in the Hengill geothermal system. Tectonics earthquakes are called as such when they are located outside the network in the catalogues.

The rate of seismicity is about more than 4 events a day (Figure 6) with periods of several earthquakes per minutes (for example 22nd of July).

The detailed analysis of all event types is not performed in this work. In the present study, we focus on volcano-tectonic earthquakes, those having clear "pickable" P and S waves to perform the joint inversion of their location and 3-D velocity model.

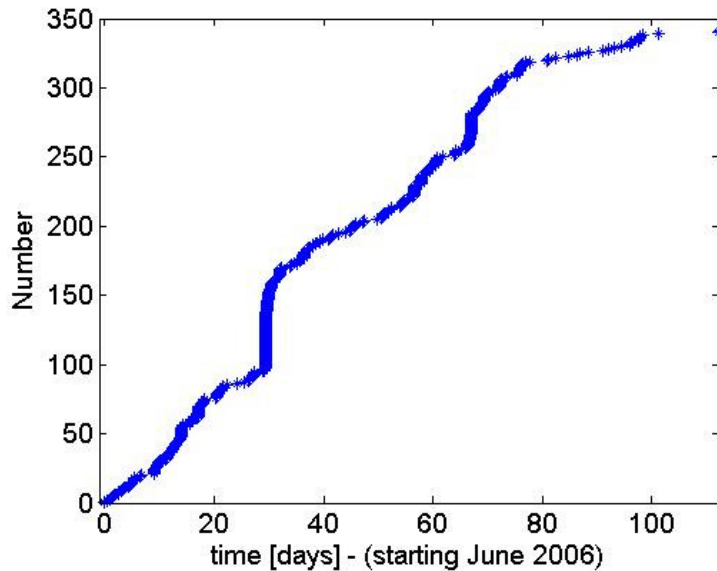


Figure 6 – Cumulative high-frequency VT seismicity at Hengill volcano recorded by IGET network from June till October 2006.

3.4. P- AND S- ARRIVAL TIMES PICKING METHOD

In order to pick the compressional (P) and shear (S) arrival times required for the tomography from the VT earthquakes, we implemented in Seismotool[®] (Jousset, 2006) an algorithm consisting in computing An Information Criteria (Akaike, 1973) directly on the amplitude vector of the seismogram (Maeda, 1985), without using autoregressive coefficients, as in standard picking techniques (Leonard & Kennett, 1999). We did not use automatic phase-picker (Allen, 1982; Zhang et al., 2003) in order to have a better control on our data set and to apply the method also to the picking of S-wave, which are more difficult to be picked accurately, automatically.

When selecting windows where a wavelet is located, the onset is the point where the AIC has a minimum value. For a seismogram $x[1,N]$ of length N , the AIC value is defined as

$$AIC(k) = k \log \{var(x[1,k])\} + (N-k-1) \log \{var(x[k+1,N])\}, \quad (1)$$

where k ranges through all the seismogram samples. This AIC picker defines the onset point as the global minimum. For this reason, the time window must be chosen to include the segment of seismogram of interest only. For a very clear P-wave onset in the seismogram (Figure 7), AIC values have a very clear AIC global minimum at the sample where the P-wave is thought to begin. For a low signal to noise ratio, the global

minimum is not giving satisfactory results. In addition, our broadband data includes also oceanic micro-seism, which affect the AIC values, preventing accurate picking to be obtained, unless filtering is applied. Nevertheless, this picking method minimizes errors due to change of operator and bias due to habit of a single operator after many picking.

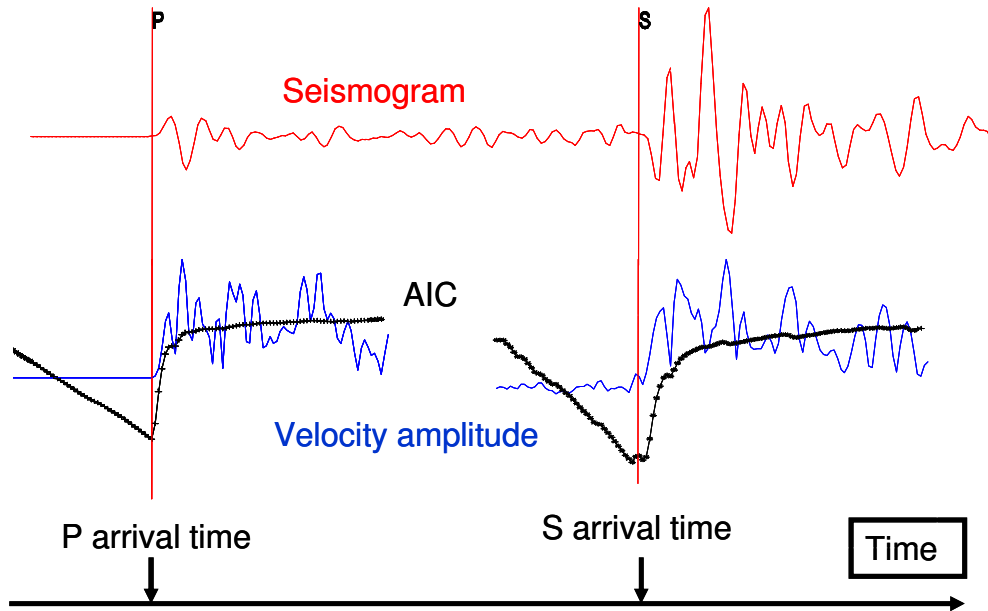


Figure 7 – Akaike Information criteria semi-automatic picking method.

Error estimation on picking is also implemented in Seismotool. The error is estimated by the use of two picking values instead of only one as usually done. The two picked times define a time interval during which the wave arrival time might be located with uniform probability.

3.5. PHASES STATISTICS

Table 3 indicates the repartition of the picked phases used for the joined inversion of the earthquake hypocenters and velocity model. Figure 8 shows the statistics on P and S picks, revealing the quality of our data set.

	HE1	HE2	HE3	HE4	HE5	HE6	HE7	HEI	KRO	SAN	Total
P	230	244	194	309	233	304	215	149	243	145	2266
S	262	293	297	324	205	313	237	113	258	130	2432
Total	492	537	491	633	438	617	452	262	501	275	4698

Table 3 – Number of picks for IGET network at Hengill volcano.

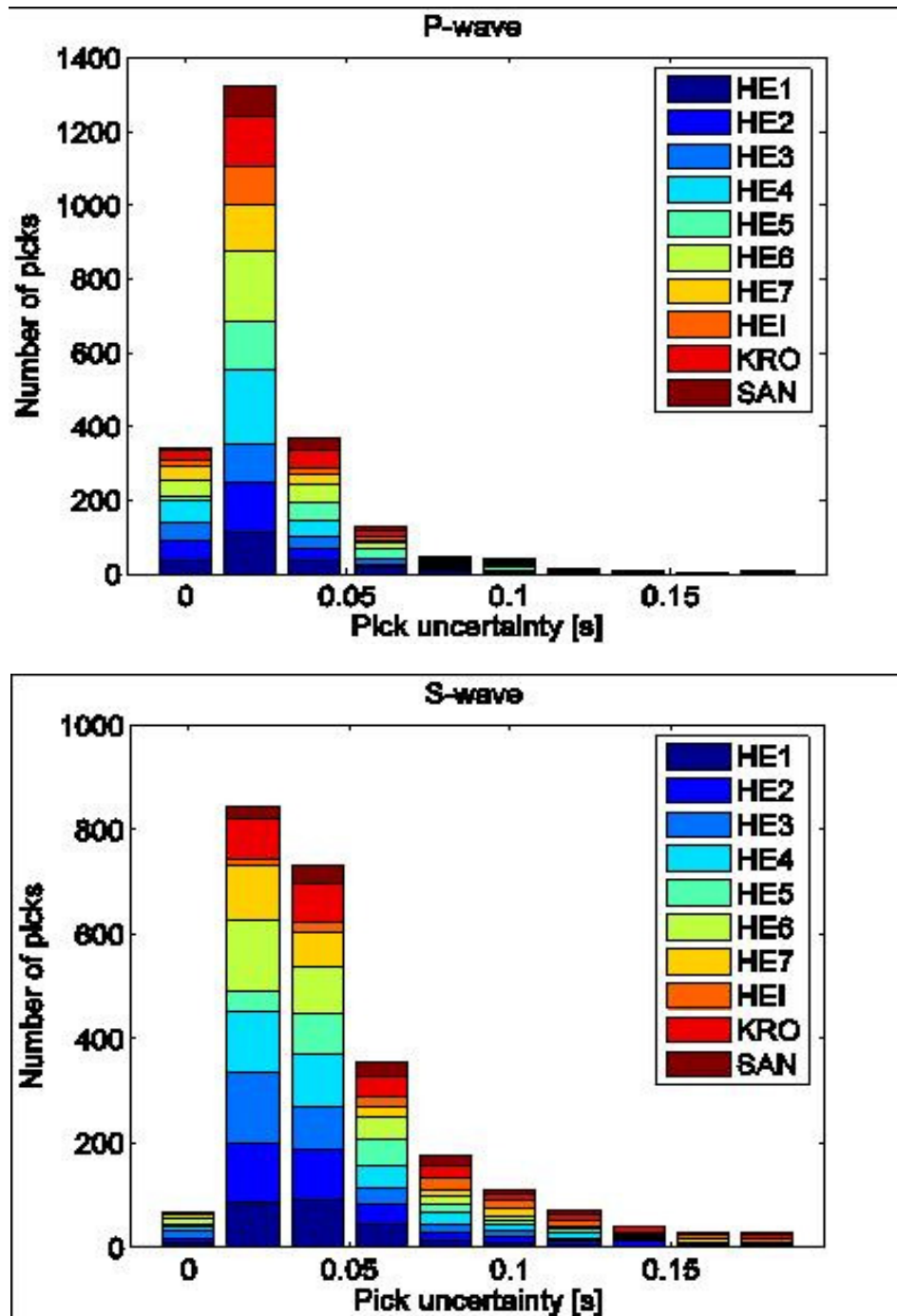


Figure 8 – Statistics on the (left) P and (right) S picks. About 4800 picks were performed, with 80% and 65% being below 0.05 s for P and S waves, respectively.

4. Joint inversion of hypocenter location and 3-D velocity model for Hengill area

4.1. PREVIOUS STUDIES AND METHODOLOGY

The structure of the Hengill region has been studied using geological and tectonic and seismological 3-D tomography techniques by a number of authors (Foulger, 1988a; Foulger et al., 1989; Foulger et al., 1995; Saemundsson, 1995; Evans et al., 1996, Julian et al., 1997; Miller et al., 1998, Tryggvason et al., 2002), together with studies concerning processes using source mechanism (Foulger & Long, 1984; Foulger, 1988b; Foulger & Toomey, 1989; Miller et al., 1998) or analysis of swarms (Sensschönfelder et al., 2006).

For instance, in 1981, a temporary network of 23 analog seismic stations with vertical component seismometers recorded 2000 locatable earthquakes (Foulger, 1988a, Foulger 1995), from which a three-dimensional variation of P-wave speed v_P was obtained (Toomey and Foulger, 1989; Foulger & Toomey, 1989) with a resolution of 2 km horizontally and 1 km vertically. In 1991, a temporary network of 30 seismic stations with Mark Products L22D 2 Hz, three-component sensors and REFTEK data loggers recorded ground motion continuously with a sampling rate 100 Hz for two months. 4000 earthquakes were recorded. Inversion of 228 well-distributed earthquakes and one explosion allowed (Foulger et al., 1995; Miller et al., 1998) to apply classical seismological tomography methods. In this case, the analysed volume was 3 times larger than the volume analysed in 1981, but the resolution was not improved. Those local tomography studies from micro-earthquakes within Hengill geothermal system provided us with a velocity model for both P and S waves (Miller et al., 1998). Those models ranges a 24*24 km² area about the origin of the models at lat = 64° 02' 45"; lon = 21° 17' 30" in geographic coordinates or northing 7102154 m; easting 485757 m in UTM coordinates (Zone 27), covering thus perfectly the area of our network. However, velocity values are sampled every 2 km. Tryggvason et al. (2002) used 9 years of the SIL records comprising about 75000 earthquakes to perform the tomography of Southwest Iceland, with special interest at Hengill triple junction. The resolution of the model is 4*4 km. Resolutions of those velocity models are not sufficient for the study of details in the geothermal field.

4.2. METHODOLOGY

Our network comprised 2 CMG-40TD (0.016-50 Hz) Güralp and 5 CMG-ESP (0.008-50 Hz) broadband stations comprising 3-components seismometers. Data digitized with a sampling rate of 100 Hz was stored on high capacity local hard disks. The network recorded ground motions from the 25th of June till the 20th of October 2006. A detailed description of the broadband network, station set-up and data processing can be found in (Jousset & François, 2006; Jousset et al., 2007; Jousset et al., 2008a, 2008b, 2008c). In addition, we used 3 stations from the permanent Icelandic network

(Stefansson, 1993), set to record continuously data during the 4 months of recording of the broadband network (Table Table 1).

We used 339 micro-earthquakes with clear P- and S- arrival times to image the compression P-wave and shear S-wave structure of the geothermal reservoir applying tomography inversion to the 2266 P- and 2432 S- waves arrival times with the computer program SIMULPS12 (Evans et al., 1994), which solves simultaneously for earthquake locations and crustal structure by the iterative damped-least-square method. The program VELEST (Kissling, 1994) provides one-dimensional v_P (and v_S) models used as a starting point for the inversion. A careful choice on the earthquakes and inversion parameters has been done prior to the inversion (Eberhart-Phillips, 1993).

4.3. V_P/V_S RATIO FROM WADATI DIAGRAM ANALYSIS

The v_P/v_S ratio can be determined by using the Wadati diagram in which the S-P interval time is plotted against the P-arrival time, t_P (Wadati, 1933). It is a first indication of the mean v_P/v_S ratio which can be used

- for detecting outliers in picked arrival times
- as *a priori* information for tomographic inversions.

We follow the approach of Chatterjee et al. (1985) in which the S-travel time is plotted against the P-travel time in order to estimate the v_P/v_S ratio from the data set. In this approach, the propagation time Δt_P of a P- wave in a medium of constant velocity v_P between the source hypocenter of an earthquake 'eq' happening at a time t_{eq} and the receiver R recording the wave at the arrival time t_P reads by definition $\Delta t_P = d_P/v_P$, d_P being the distance of the path way of the wave. The same applies for the S-wave. Assuming to the first order that the path of the P-wave and the path of the S-wave is the same, we deduce the $r = v_P/v_S$ ratio as being defined by the ratio of the S-wave travel time to the P-wave travel time. Therefore, picked P and S arrival times have to align themselves along a straight line in a homogeneous medium. Variations about the straight main line reflect velocity anomalies in the crust. In addition, once the ratio has been derived for an earthquake, it is possible to approximate the time of the earthquake as $t_{eq} = [1/(1-r)] (t_P - t_S)$.

The Wadati diagram allows also to remove clear outliers, when points (t_P, t_S) are clearly outside the line defining the v_P/v_S ratio. These outlier points are most of the time due to either bad P- or S- picks or both. For those points, instead of removing them from the data set, we got back to the seismogram waveforms and verified (and corrected) the picks. In our data set, errors were mainly due to errors on the S- wave picks (about 25 bad picks) for remote stations (HEI and SAN), probably due to S- to P- wave conversions, and errors on the P- or/and S- picks, due to too low amplitude signal/noise ratio.

After the bad picks have been corrected, our data set comprises 339 earthquakes. The Wadati diagram analysis was applied to this filtered data set leads to $v_P/v_S = 1.75 \pm$

0.12 (Figure 9). We also computed the ratio for each earthquake separately and took the average value of all individual ratios. We found $v_P/v_S = 1.76 \pm 0.15$. These values are similar to the v_P/v_S ratio found from previous data analysis in Hengill area. Foulger et al., 1995 and Miller et al., 1998 found $v_P/v_S = 1.77$ and Tryggvason et al., (2002) found $v_P/v_S = 1.78$.

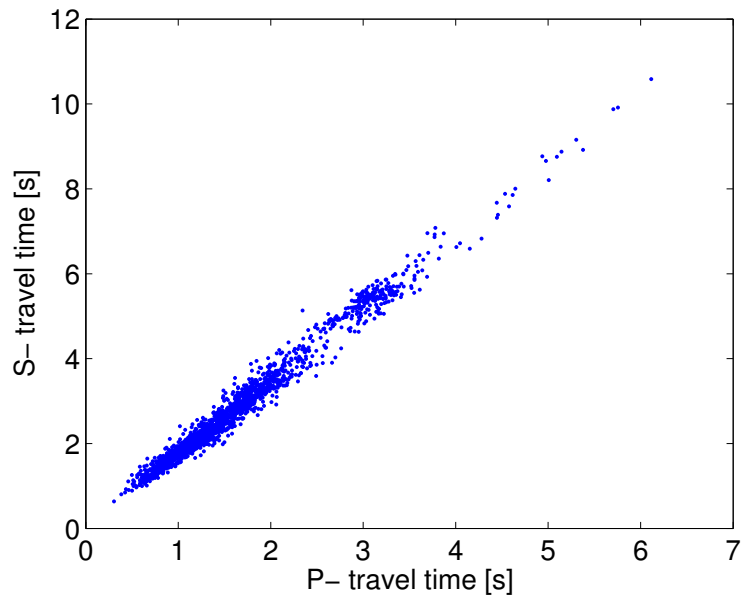


Figure 9 – Wadati diagram on 339 earthquakes of IGET network at Hengill.

4.4. JOINT HYPOCENTER LOCATION AND 3-D MODEL TOMOGRAPHY INVERSION

We inverted our high quality data set comprising 339 earthquakes detected by at least 4 stations using models of increasing complexity. Many tomographic studies (Thurber, 1983; Eberhart-Phillips, 1990; Eberhart-Phillips & Michael, 1993; Eberhart-Phillips, 1998) simultaneously invert local earthquakes arrival times for hypocenters locations and 3-D velocity structure, in two steps:

1. joined inversion for 1-D velocity model and hypocenter locations
2. joined inversion for 3-D velocity model and hypocenter locations

We performed in addition a preliminary step, in order to increase the resolution of our model as shown below.

4.4.1. *a priori* hypocenter location for inversion and methodology

We performed first two preliminary independent hypocenter location inversions using a homogeneous model for P-waves with a velocity of 5 km/s for inverting P-picks only,

and a homogeneous model for S-waves with a velocity of 3 km/s for inverting S-picks only. The P- and S- velocity values used are average values taken from previous studies at Hengill (Foulger et al., 1995; Miller et al., 1998; Tryggvason et al., 2002). These two preliminary inversions were implemented and performed in Seismotool (Jousset, 2006), by computing travel times at each station for sources located at regularly spaced nodes of 3-D grid spanning the whole area of Hengill volcano up to 10 km depth.

For example, for P-wave travel times, Figure 10 shows that the first order locations of the earthquakes fall in the area of our network. We also performed an inversion with the S-wave travel times only and homogeneous velocity under the free-surface topography. Both inversions reveal a similar distribution pattern of hypocenter locations and are located in a plane perpendicular to the direction of the rift.

Using (or not) the *a priori* hypocenter locations previously computed, the two-step tomography approach using the 1-D model inversion code VELEST (Kissling, 1994) and 3-D model inversion code SIMULSP12 (Thurber, 1993; Evans et al., 1994) was then performed. One requirement of SIMULPS12 is that the earthquakes must lie within the aperture network. This means that earthquakes located outside the network cannot be used. The usable data set is reduced to 263 earthquakes. Note, however, that we used all earthquakes for the joined 1-D inversion, as this requirement is not relevant.

Another approach is based on the inversion code TOPOS (Kulakov et al., 2007) and could use all earthquakes. This approach was not performed and therefore not described in this report.

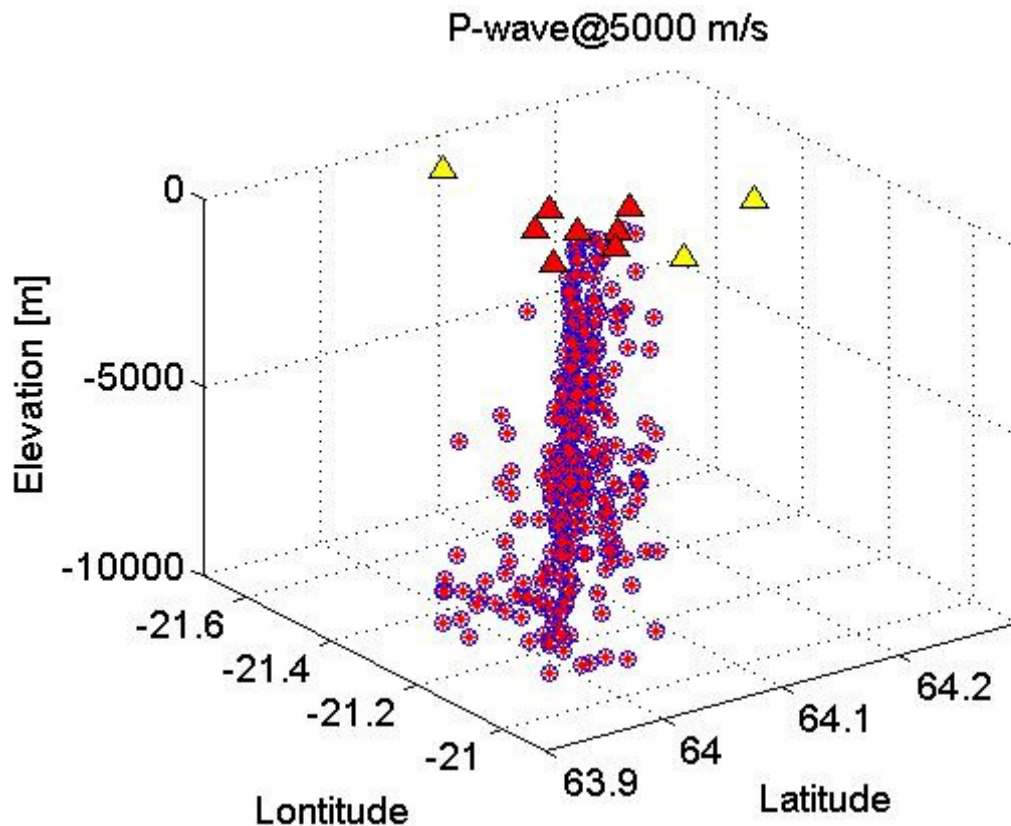


Figure 10 – Hypocenter locations of the 339 earthquakes obtained by the grid search inversion of the P-wave travel times assuming an homogeneous medium with $V_p=5000$ m/s.

4.4.2. VELEST 1-D inversion

The first step consists in performing a joint inversion for hypocenter locations of the 339 detected earthquakes, 1-D velocity model and station corrections using VELEST (Kissling, 1994). Note that we may use the *a priori* hypocenter locations inverted using Seismotool (Jousset, 2006), or not. In the later case, we set all the hypocenters to an *a priori* depth of 4000 m and epicentres below the centre of the network, at the station HE3. For each case, we inverted for the v_p model using either P- or S- arrival times or both, and assuming a constant average v_p/v_s ratio of 1.765 (based on the previous Wadati diagram analysis, see Figure 9), and using a wide range of starting velocity models, to estimate the resolution of the 1-D inverted model.

v_p 1-D model

The usual approach starts by inverting the P-wave velocity v_p model first, using P-wave arrival times and/or S-wave arrival times. An initial test indicates that the use of P-wave arrival times only leads to improbable results (P-wave velocity too small) (Figure 11 and Figure 12). Therefore, we used P- and S- arrival times for all following inversions. In the case where we did not use the *a priori* hypocenter positions obtained from the

grid search hypocenter determination, we run two inversions with two different *a priori* hypocenter locations (Figure 13 and Figure 14). These figures demonstrate that *a priori* hypocenter locations have a strong influence on the inversion results, both in terms of the velocity model profile and value and hypocenter location at Hengill complex. Therefore, in the following, we used the *a priori* hypocenter locations for all inversions. The final results of the 1-D inversion using *a priori* hypocenters obtained from the preliminary inversion (shown in Figure 10) are shown in Figure 15 using P- arrival times only, for completeness, and in Figure 16 using P- and S- arrival times. This last P-wave velocity model (Figure 16) is used as *a priori* information for inverting the v_P/v_S ratio. It is interesting to note that the locations of the earthquakes are kept rather constant in the area of the network, validating the first order result obtained.

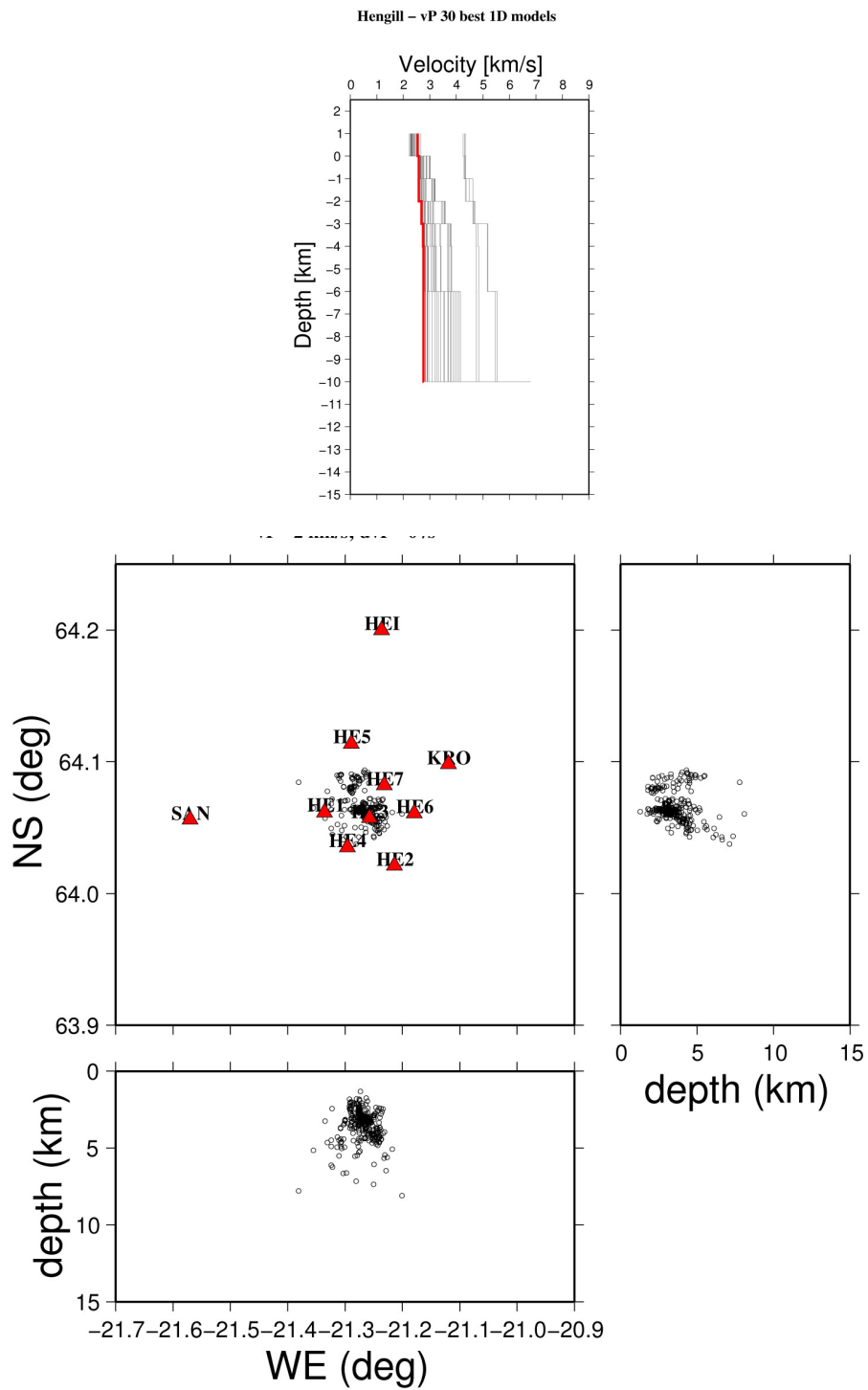


Figure 11 – (top) Inverted 1-D P-wave velocity v_P 30 models with lower RMS and (bottom) 339 earthquake hypocenter locations using P-wave arrival times only. The a priori location is below HE3 station at 4 km depth. Left: inverted; best model (lowest RMS) in red. Triangles: IGET network and SIL stations locations.

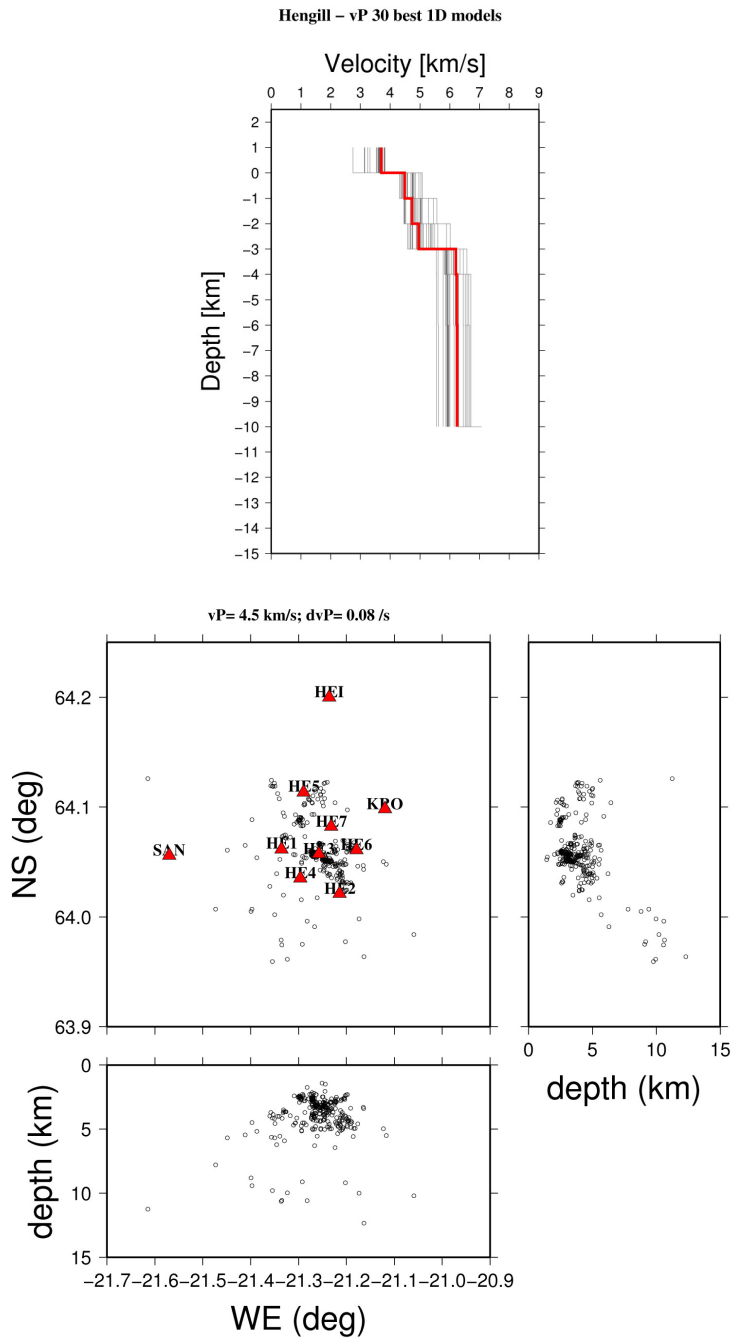


Figure 12 - (top) Inverted 1-D P-wave velocity v_P 30 models with lower RMS and (bottom) 339 earthquake hypocenter locations using P- and S-waves arrival times. The a priori location is below HE3 station at 4 km depth. Left: inverted; best model (lowest RMS) in red. Triangles: IGET network and SIL stations locations.

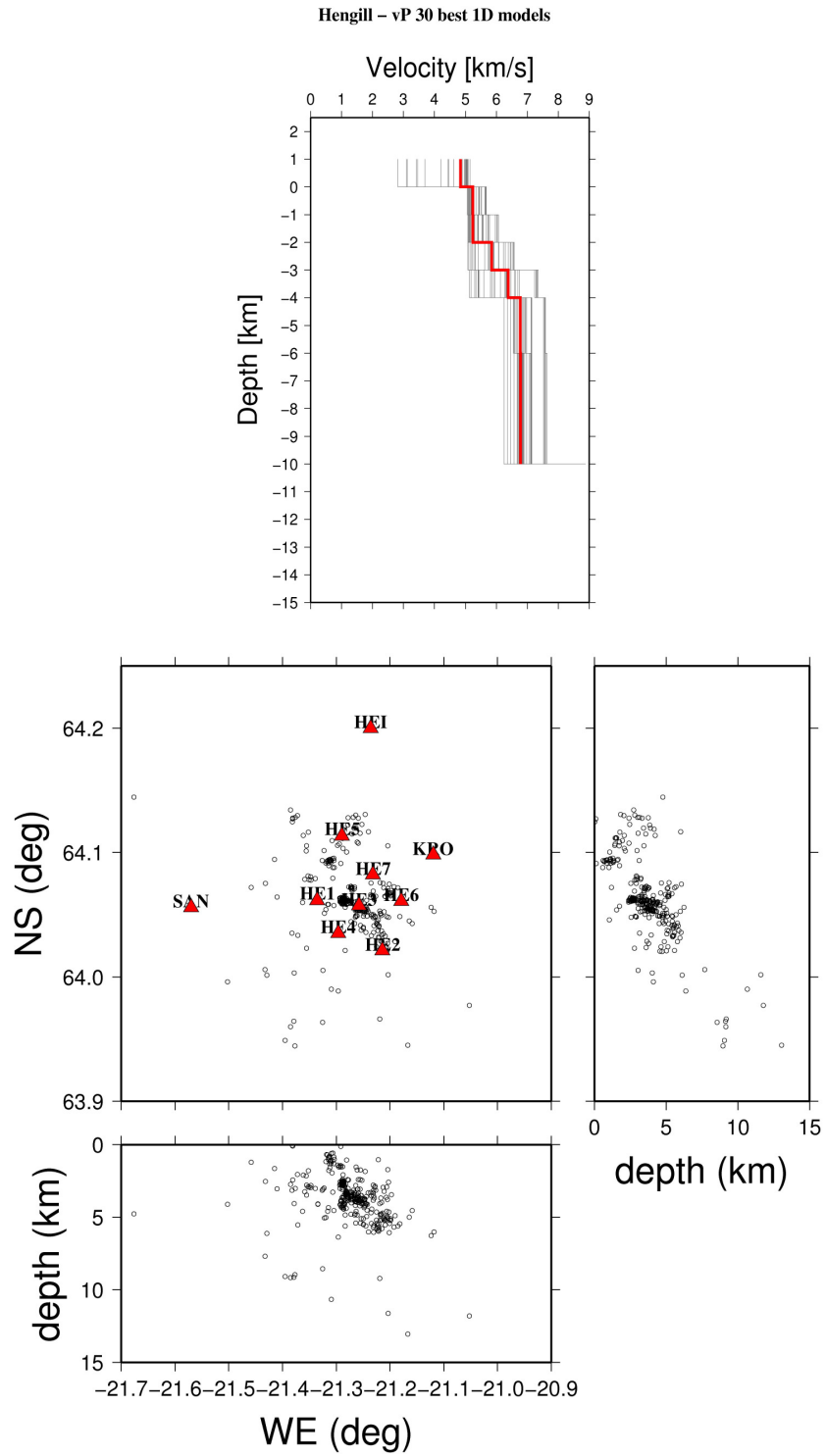


Figure 13 - Inverted 1-D v_P models using fixed hypocenter location (339 earthquakes). A priori hypocenter location at lat=64.0N; lon=21.5W - depth 4 km.

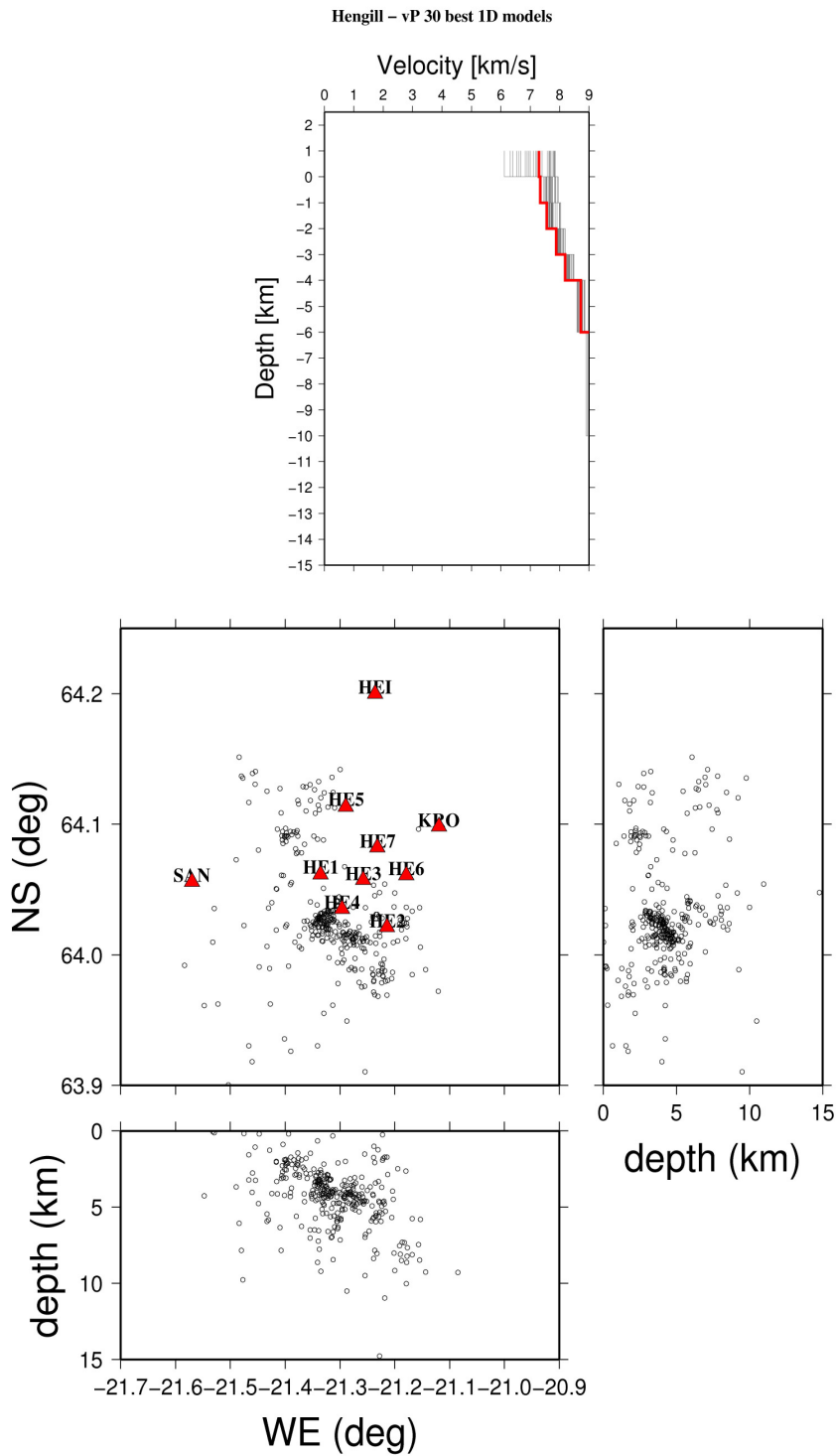


Figure 14 – Inverted 1-D v_P models using fixed hypocenter location (339 earthquakes). a priori hypocenter location outside network aperture at lat=64.1N; lon=21.4W - depth 4 km. Compare with Figure 11 bottom results with HE3 a priori location.

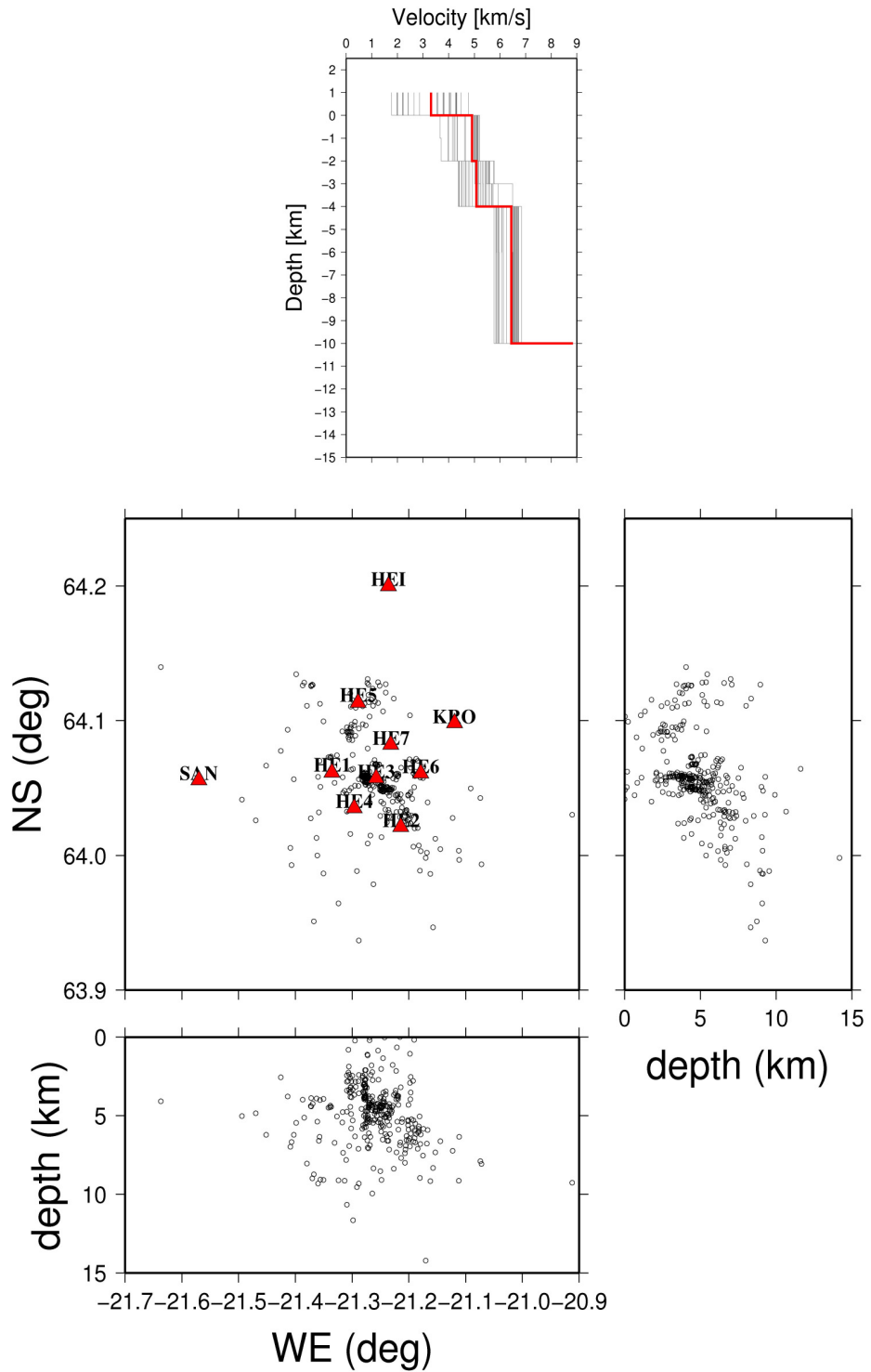


Figure 15 - Inverted 1-D v_P models using a priori locations from the preliminary inversion using P -arrival times only.

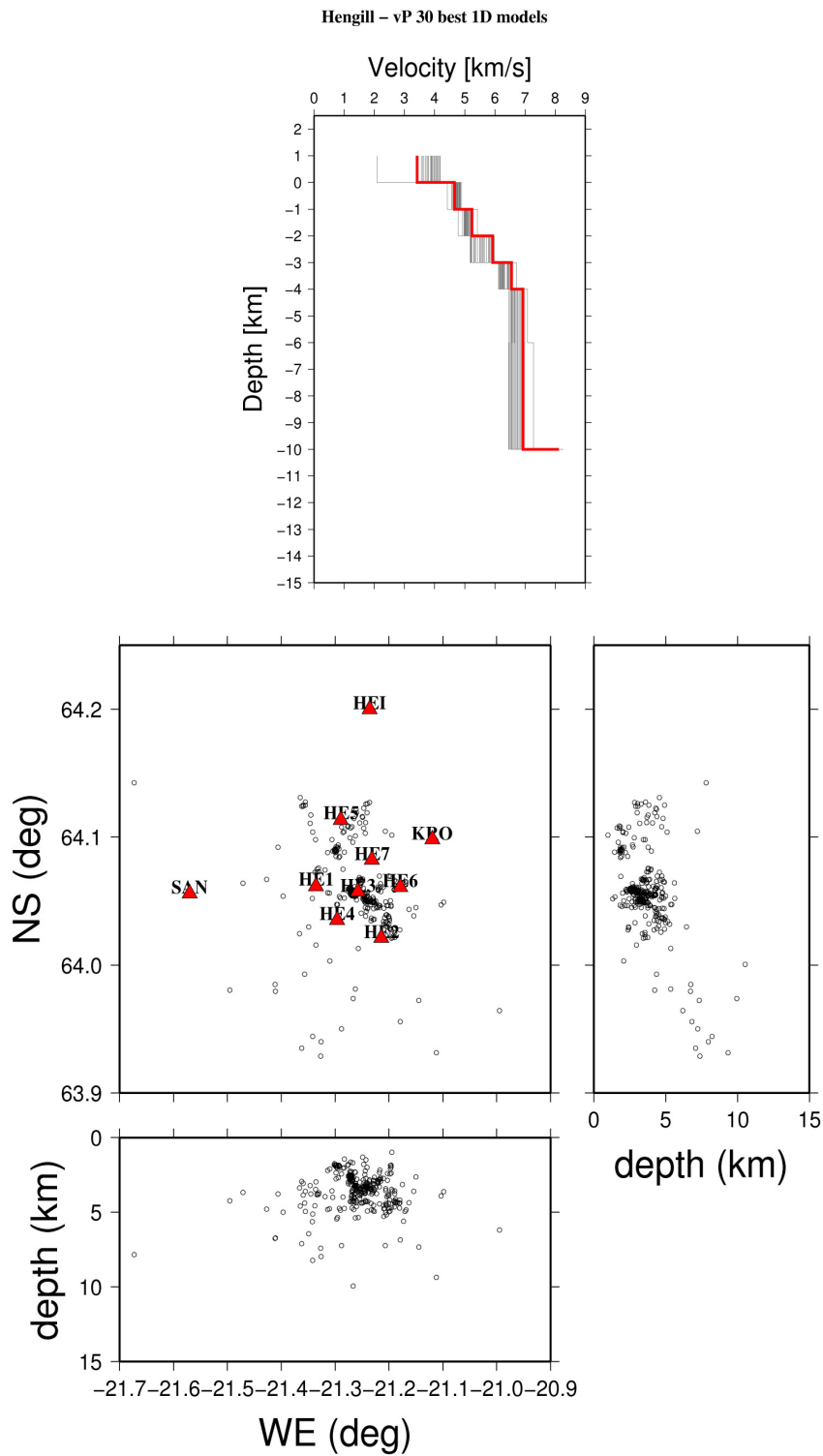


Figure 16 - Inverted 1-D v_P models using a priori locations from the preliminary inversion (top) using P- and S- arrival times. This model is the one used for further inversions.

Data variance from the inversion for the 1-D model is $RMS=0.41349$. The analysis of station corrections leads us to conclude that because these corrections are small (to the first order), the inverted hypocenters are rather accurate. In addition, stations corrections (Table 4) are systematically positive for the stations (HEI, KRO and SAN) located outside Hengill volcano, whereas station corrections within the network (HE1 to HE7) are all negative. This observation may point to 3-D structural features (Haberland et al., 2006).

Stations	location	Station correction [s]
HE1	64.0615N 21.3358W 473	-0.08
HE2	64.0212N 21.2142W 83	-0.16
HE3	64.0573N 21.2577W 390	-0.29
HE4	64.0350N 21.2960W 375	-0.21
HE5	64.1135N 21.2892W 373	0.00
HE6	64.0610N 21.1792W 373	-0.16
HE7	64.0822N 21.2317W 360	-0.16
HEI	64.1998N 21.2361W 162	0.22
KRO	64.0981N 21.1198W 147	0.10
SAN	64.0560N 21.5701W 208	0.19

Table 4 – Stations corrections computed in the inversion leading to the best v_P model.

v_P/v_S ratio 1-D model

The same approach is used to invert for the v_P/v_S ratio 1D model. Table 5 gives the final v_P velocity 1-D model used for the 3-D inversion, and results of the corresponding v_S velocity model and v_P/v_S ratio 1D model. It is hazardous to use the v_P/v_S ratio 1D model as such. Experience (Haberland, pers. comm.) suggests that we should use the v_P 1-D model as an initial model for the 3-D inversion and not for any preliminary interpretation. It is however interesting to note that a low v_P/v_S ratio anomaly results from the inversion at shallow depth, which is consistent with results from Tryggvason et al. (2002).

Depth [km]	V_P [km/s]	V_S [km/s]	v_P/v_S ratio
-1	3.21	1.25	2.57
0	4.67	1.69	2.76
1	4.68	2.79	1.68
2	5.30	3.28	1.62
3	6.01	3.38	1.78
4	6.45	3.84	1.68
6	6.62	3.85	1.72
10	7.76	3.85	2.01

Table 5 – Results of the 1-D inversion.

4.4.3. 3-D inversion using SIMULPS12

We performed 3-D tomography using SIMULSP12 (Evans et al., 1994). As pointed out by Evans et al. (1994), we first filtered out all events which were "outside" our network using the 'gap' parameter, i.e, removing all earthquakes which greatest angle between any two stations being greater than 180 degrees. The number of earthquakes in the reduced data set is 269 earthquakes. We used the final 1-D v_P model and we varied v_P/v_S values as starting models in subsequent inversions. The structure is parameterized by the values of the P-wave velocity v_P and the v_P/v_S ratio at the nodes of a 3-D grid, and the observed P- and S- arrival times are inverted by an iterative least-squares method to determine simultaneously the coordinates of earthquakes hypocentres and the values of v_P and v_P/v_S ratio at the grid nodes. Tri-linear interpolation is used between nodes for v_P and the v_P/v_S ratio between the nodes. The ray path are calculated with an approximate 3-D ray tracing algorithm that produces curved, non planar ray paths, which are defined by points more finely spaced than the velocity grid. The solution is obtained by iterative damped least squares inversion. For each iteration, new ray paths are determined, the hypocenter solution is included, and parameter separation is performed. Weighting is applied to each observation based on the size of the travel time residual and source-receiver distance. The full resolution matrix is calculated (Yao, 1999).

Trade-off curve

A damping parameter is used to stabilize the inversion (Eberhart-Phillips, 1986; Haberland, 2006). If the damping is not used (equivalent to damping=0), then the inversion produces instabilities such that spatial oscillations of the velocity appear in result, which do not correspond to geophysical significance. In order to avoid such oscillations, an increased damping value is used. If the damping is too large, then there are no velocity variations in the model and the 1D velocity model is kept; in such a case, data variance is very large (with a maximum being the data variance for 1-D velocity model), as the 3D velocity variations are not properly modelled. There exist therefore a trade-off between the data variance and the model variance to be found. The optimal value of the damping is the one for which the data variance is minimum. The model variance corresponds to the 3D anomalies with respect to the 1D model.

To summarize, prior to each 3-D inversion, the damping parameter is chosen empirically by evaluating a trade-off curve of data variance and solution variance as the damping varies with the model grid and the data set (Eberhart-Phillips, 1986; Haberland, 2006). Figure 17 shows an example of the trade-off curve of the damping parameter computed for a grid sampling of 2 km in the case of P-wave velocity 3-D model inversion.

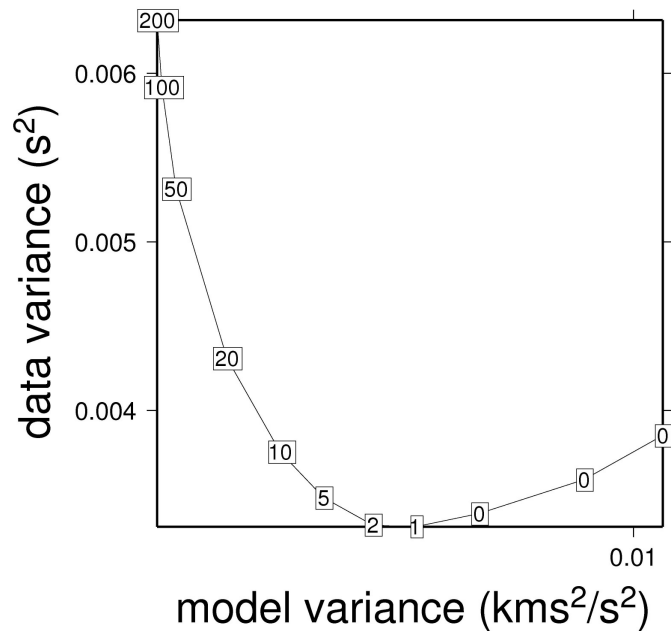


Figure 17 – Trade-off curve of the damping between the data variance and model variance for the case of 3-D v_p inversion sampled every 2 km. The damping parameter value chosen in this case will be 2.

v_p 3-D inversion

We performed a series of simultaneous hypocenter-velocity inversions progressively increasing the complexity in the model and refining the mesh of the 3-D grid. Data variance decreased after each step. We started using a coarse 3-D grid spacing of 2 km, with several nodes outside the target geothermal system, in order to constrain the volume that our data set can image. This first model has a RMS=0.04874. In a second inversion process, we refined the grid to 1-km grid spacing, in order to image more accurately the geothermal system. This second model has a RMS=0.06630.

Results are shown on cross-sections (NS and EW) and horizontal slices at different depths (Figure 18, Figure 19, Figure 20, Figure 21, Figure 22 and Figure 23). Comparisons between the inversion results and resolution analysis for inversion grid spacing show that a grid spacing of 1 km is a spacing that produces excellent image fidelity without serious loss of resolution for the critical region directly below our network. A more complete analysis would be to decrease smoothly the grid spacing and compare the loss of model resolution and variance. The same approach has been used to compute the v_p/v_s ratio.

Broadband seismicological network at Hengill

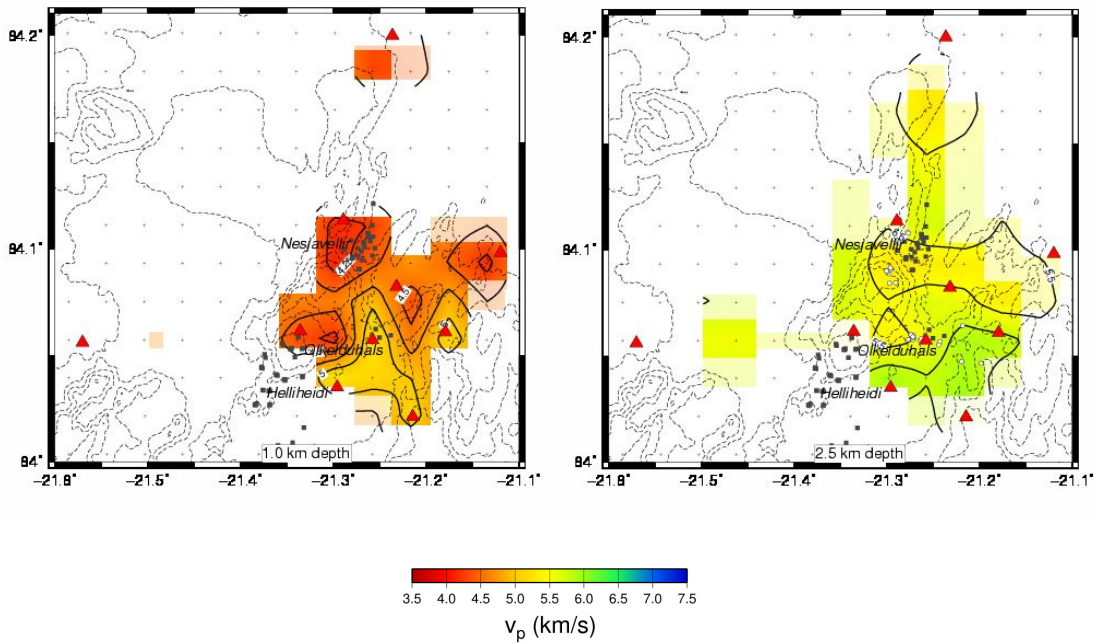


Figure 18 – Horizontal slices of P-wave velocity 3-D tomography inversion at Hengill using a grid of 2 km. Triangles represent station locations. Continuous lines indicate constant velocity. White circles represent earthquake location within a $-0.5/+0.5$ km range from the slice depth.

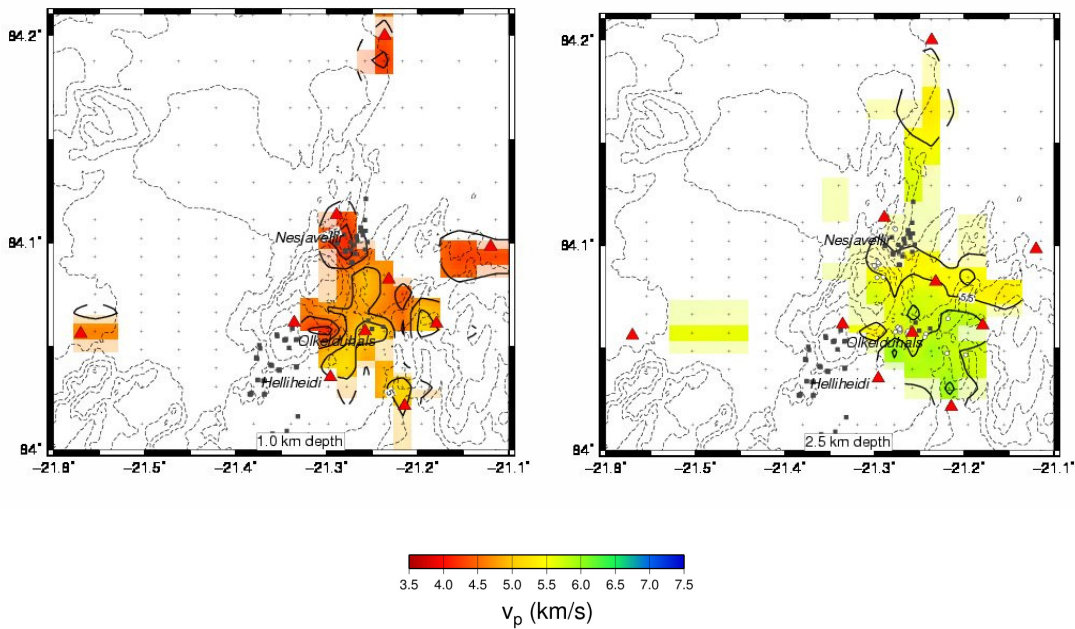


Figure 19 - Horizontal slices of P-wave velocity 3-D tomography inversion at Hengill using a grid of 1 km. Triangles represent station locations. Continuous lines indicate constant velocity. White circles represent earthquake location within a $-0.5/+0.5$ km range from the slice depth.

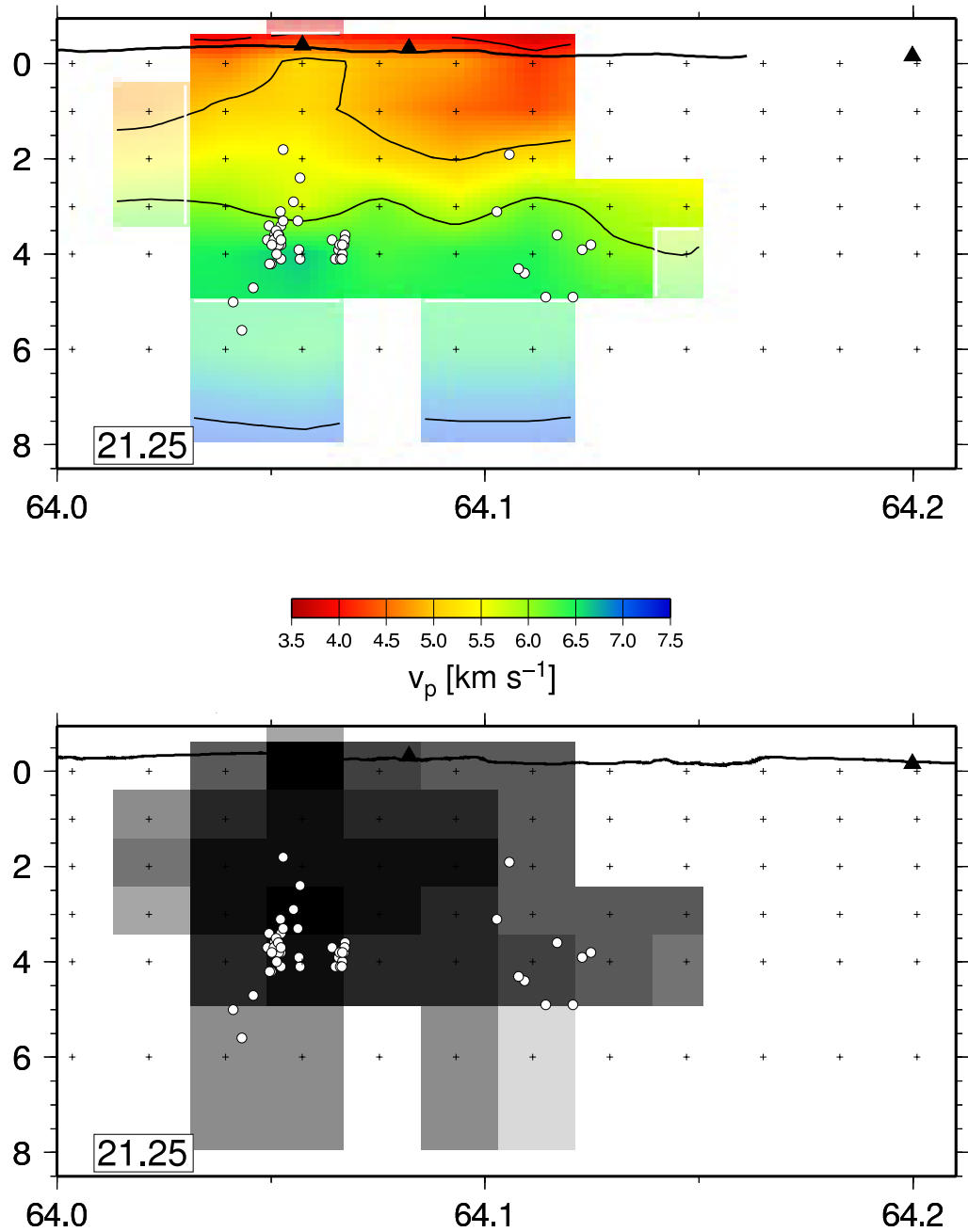


Figure 20 – E-W cross-sections of (top) P-wave velocity at Hengill geothermal system from the 3-D tomography inversion with a grid of 2 km. Continuous lines indicate constant velocity. (bottom) spread values of the tomography. Dark shading (low spread values) in the center of the model volume indicate a good resolution. The outer regions show a reduced resolution as indicated by lighter shading. Triangles represent station locations at the surface indicated by a thick black line. White circles represent earthquake location within a $-0.05/+0.05$ degree range from the position of the cross-section.

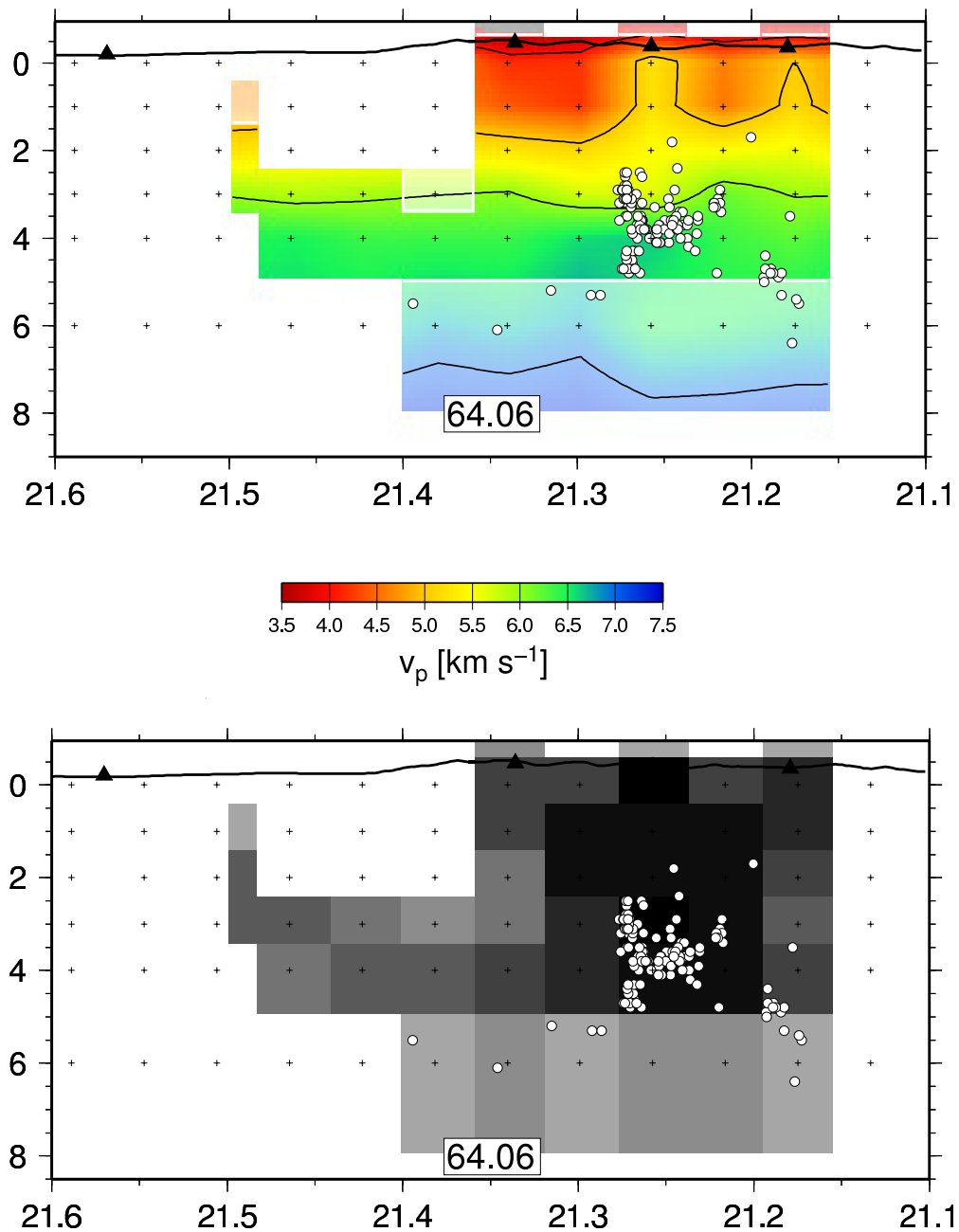


Figure 21 – N-S cross-sections of (top) P-wave velocity at Hengill geothermal system from the 3-D tomography inversion with a grid of 2 km. Continuous lines indicate constant velocity. (bottom) spread values of the tomography. Dark shading (low spread values) in the center of the model volume indicate a good resolution. The outer regions show a reduced resolution as indicated by lighter shading. Triangles represent station locations at the surface indicated by a thick black line. White circles represent earthquake location within a $-0.05/+0.05$ degree range from the position of the cross-section.

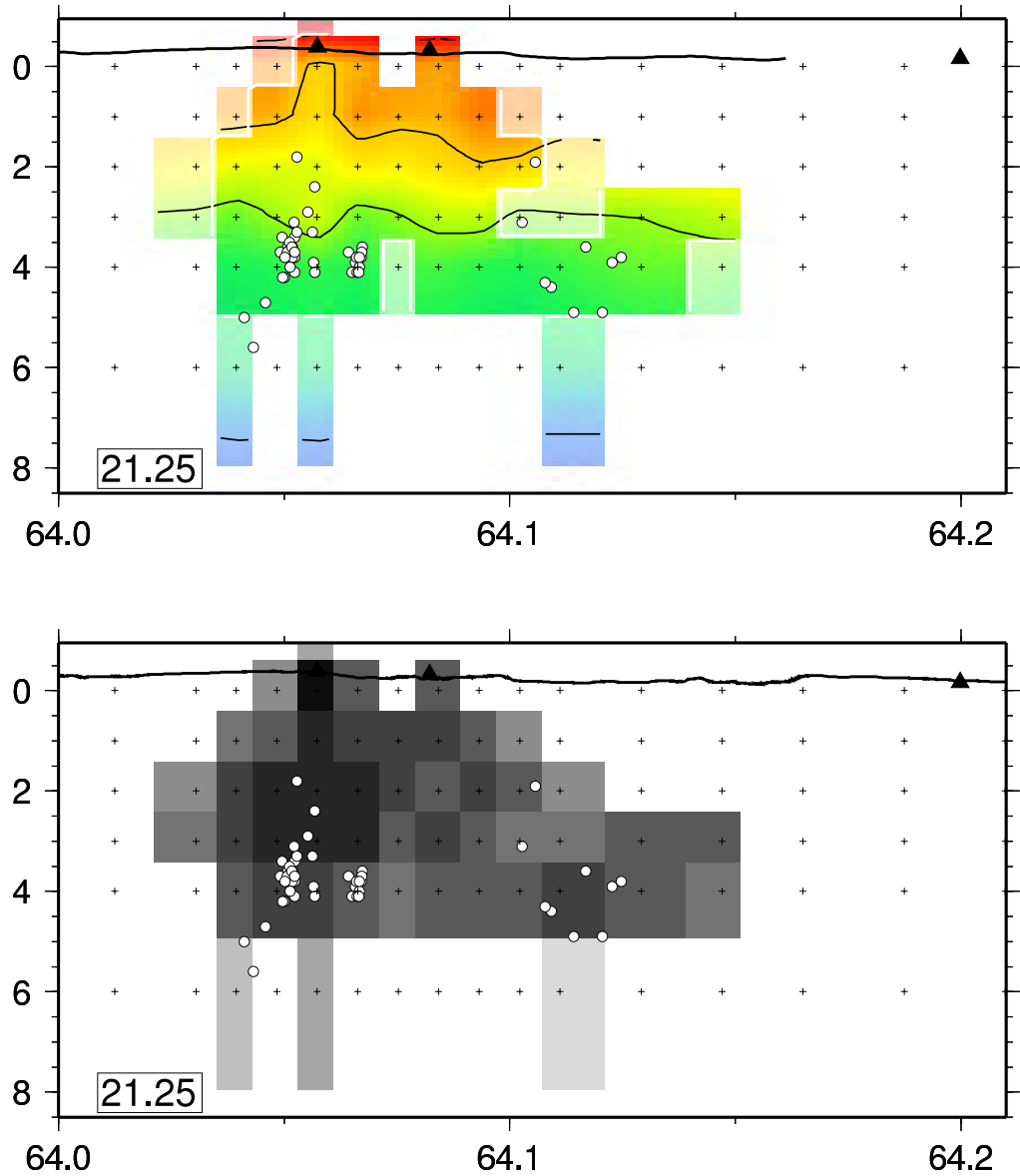


Figure 22 - E-W cross-sections of (top) P-wave velocity 3-D tomography inversion at Hengill using a grid of 1 km. Black triangles represent station locations at the surface indicated by a thick black line. Continuous lines indicate constant velocity. (bottom) spread values of the tomography. Dark shading (low spread values) in the center of the model volume indicate a good resolution. The outer regions show a reduced resolution as indicated by lighter shading. White circles represent earthquake location within a $-0.05/+0.05$ degree range from the position of the cross-section.

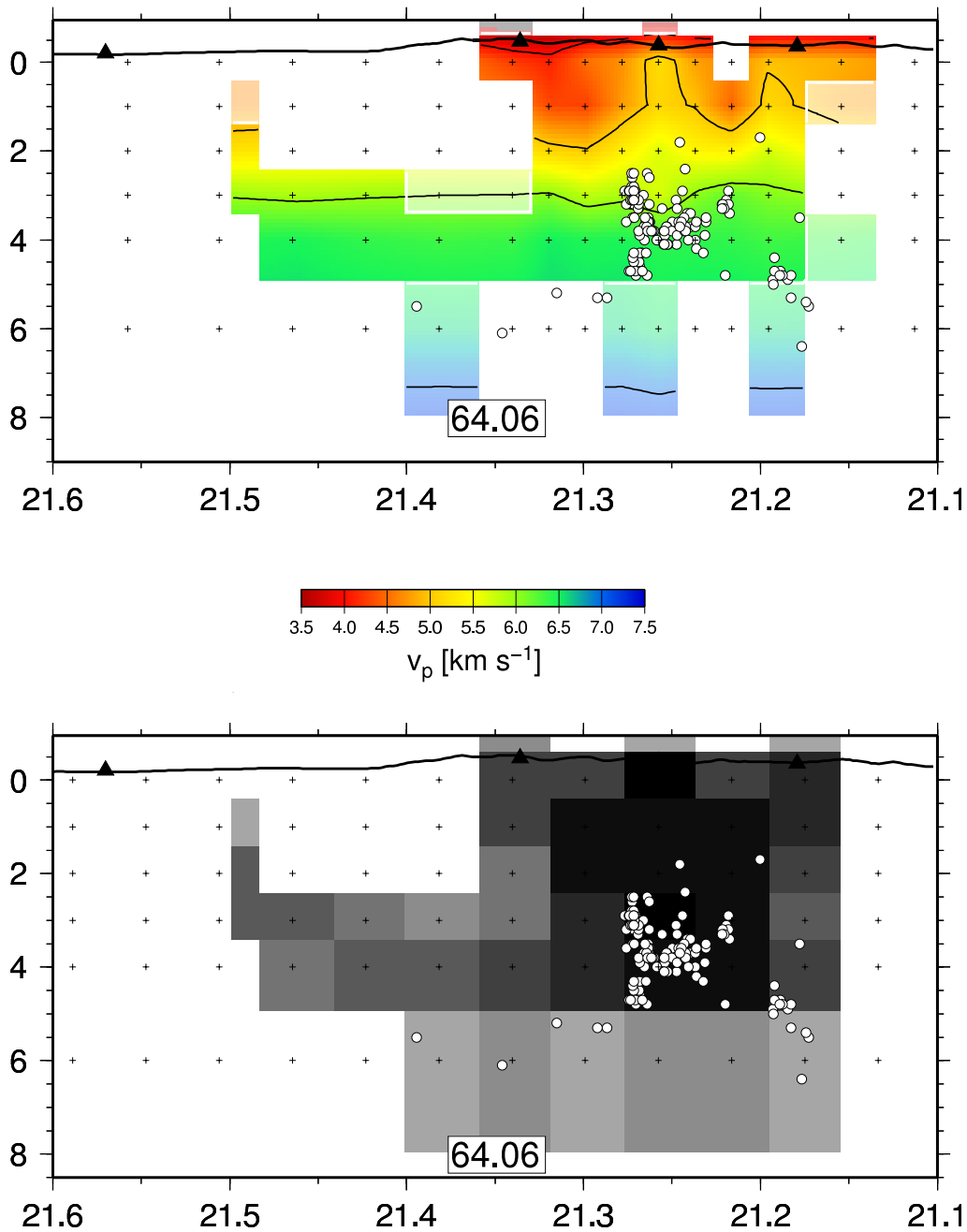


Figure 23 - E-W cross-sections of (top) P-wave velocity 3-D tomography inversion at Hengill using a grid of 1 km. Black triangles represent station locations at the surface indicated by a thick black line. Continuous lines indicate constant velocity. (bottom) spread values of the tomography. Dark shading (low spread values) in the center of the model volume indicate a good resolution. The outer regions show a reduced resolution as indicated by lighter shading. White circles represent earthquake location within a $-0.05/+0.05$ degree range from the position of the cross-section.

Event re-localisation using HYPODD

After the last 3-D inversion has been performed, we further improved the location of the earthquake by using the double-difference technique (Waldhauser & Elsworth, 2000). We also compared with results from relocations of earthquakes using the same double-difference technique, but from the initial joint hypocenter/1-D model inversion. The improvement in the variance reduction is further improved.

3-D final inversion

Finally, using the relocated earthquake positions and starting from the best 3-D velocity model, we performed an ultimate 3-D inversion to adjust the final velocity model and final hypocenter positions. Note that the data variance decreases all along our inversion strategy.

Resolution and robustness of models

The resolution matrix describes the distribution of information for each node, such that each row is the averaging vector for a parameter (Thurber, 1993; Yao, 1999). It provides necessary information for interpretation regarding the distribution of ray-paths and the degree and pattern of smoothing. Estimating model fidelity or resolution in earthquake tomography may be performed by several means, e.g., inspecting the diagonal elements of the resolution matrix (Roeker, 1982), or by evaluating reconstructed synthetic models (e.g., checkerboards), for the specific geometry (Humphreys&Clayton, 1988; Eberhart-Phillips & Michael 1998). Michelini (1993) compute the resolving width, for a grid point from all the elements of the corresponding row of the resolution matrix, weighted by their distance from the grid point. This measure also takes into account how much smearing into adjacent nodes is present. Figure 20 to Figure 23 show these spread value distribution for exemplary sections.

5. Results and discussion

Within the framework of two European projects (IGET and ENGINE), a joined study between BRGM, ISOR and GFZ has been performed in order to improve our knowledge of the Hengill geothermal system. A network of 7 broadband seismometers from BRGM and GFZ instrumental pool has been installed and the analysis of 4 months continuous data was performed together with data from the Icelandic SIL network.

The analysis of the data allowed us to record about 500 micro-earthquakes (volcano-tectonics) located within the Hengill area, 40 tectonic earthquakes originating from outside Hengill volcano and 30 events called 'long-period event', amongst which 10 were located within the Hengill area. Owing the emergent characteristics of the LP signals, their accurate location cannot be based on the P and S wave travel time inversion, and requires an accurate velocity model to be known. The quality of the picks we obtained was made possible thanks to the broad-band digital sensors.

The understanding of the complex structure of the geothermal system beneath Hengill volcano and its relationship with seismicity requires independent estimates of both P- and S- velocity variations, and of v_P/v_S ratio. We used tomography techniques (e.g., Haberland et al., 2006) to improve the resolution of the 3D velocity model structure of Hengill geothermal system. Results reveal a high v_P anomaly in Okelduhals area at a depth of about 3 to 5 km and a low v_P/v_S ratio below Hengill volcano.

5.1. DISTRIBUTION OF EARTHQUAKES

Local seismic events (predominantly VT events) are found between 1 and 10 km depth beneath our network. Several individual clusters can be identified, however, most of the seismicity is located along a E-W plane slightly dipping to the South at depths ranging [2-4.5 km].

Cooling, mostly due to natural heat loss, and consequential thermal contraction and cracking in the heat source, has been proposed to be responsible for the continuous small-magnitude earthquake activity in this area (Miller et al., 1998). This mode of earthquake induction was suggested following the observation that many of the earthquakes have merely non-double-couple focal mechanisms with large explosive components (Foulger, 1984). The mechanism responsible for those non-double-couple may be fluid flow into newly formed cracks (Miller et al., 1998; Sens-Schönfelder, 2006). Tryggvason (2002) report clusters of deep earthquake to occur below the brittle layer, and relate their occurrence to a change in the strain rate of the spreading rift. We did not observe such deep earthquakes during our experiment. This suggests that the strain rate was normal during the 4 months of our experiment.

5.2. VELOCITY STRUCTURE

The understanding of the structure of the geothermal system beneath Hengill volcano and its relationship with seismicity requires independent estimates of both P- and S-velocity variations, and of v_P/v_S ratio.

We used travel time tomography to obtain an improved 3-D velocity model of Hengill geothermal system. Our dense network installed in the Hengill region allowed to obtain an increased resolution of the tomographic model in the order of 1 km horizontally. This high resolution, however, is limited to the confined region beneath our network.

Our results reveal a high v_P anomaly body in the south-east of Olkelduhals area at depths ranging [1-4 km] and a low v_P/v_S ratio below Hengill volcano. The major structural features found are high- v_P bodies at depths ranging 0 to 4 km at the South-East of Hengill volcano. v_P varies laterally by -10% to +12% from its average value within each layer. We find a low velocity body beneath Mount Hengill at shallow depth.

Foulger (1995) found a small (about 5 km³) low v_P velocity (about -7 %) beneath the northern edge of Mount Hengill that they interpreted as a small volume of partial melt, but this body was not confirmed later by the tomography by Foulger et al. (1995). We are not able to confirm this body.

Our study shows that the v_P/v_S ratio varies by ± 6 % throughout the area. The most coherent anomaly involves a low v_P/v_S at 0 to 2 km depth beneath, and correlates with areas of hot springs and fumaroles. However, both P- and S- waves velocities are drastically reduced beneath the striking fissure swarm in the Hengill area, with velocities ranging 5.9-6.3 km/s and 2.4-3.7 km/s, respectively. These results confirm the result of Tryggvason, 2002, which found a low v_P/v_S ratio area beneath Hengill, but its location is not accurate, as SIL stations are sparsely set-up around the Hengill geothermal area. This low- v_P anomaly extends at depth beneath the northern part of Mt. Hengill and to the East. Unfortunately due to the limited number of stations of our network, we cannot image the exact extension of this body at depth and to the east and west. On the basis of rock physics estimations (Norris, 1985), the interpretation of these observations is the presence of supercritical fluids rather than a large partially molten rock body.

Could we increase the resolution of the tomography at Hengill? Clearly, the ray coverage is the most important parameter required to enlarge the resolved area. For VT earthquake frequencies at Hengill (up to 30 Hz), velocities obtained at the target depth (about 6000 m/s at 4 km depth), the wavelength of those waves are about 300 m to 600 m for frequencies ranging 20 to 10 Hz, respectively. The scale parameter for our network is about 1000 to 1500 for VT earthquakes 4 km depth. Therefore, we are confident that modelling the medium with grid cell of the order of 1 km is reasonable. Trying to get a lower resolution will travel time tomography is certainly hazardous, despite we did not test it.

To better resolve the velocity anomalies, waveform tomography (Pratt et al., 1998) uses the detailed waveform data, instead of only wave travel times. We suggest that

waveform tomography would be a suitable method to further increase the resolution, while recording earthquakes with many more stations.

5.3. STRUCTURE OF HENGILL GEOTHERMAL SYSTEM

Our results confirm previous major observations from Foulger (1995), Foulger et al. (1995) Tryggvason (2002), with additional new details thanks to an increased resolution.

The integration of several geophysical techniques is another possible way to increase our knowledge of the structure of geothermal systems. Other geophysical techniques have been applied to the Hengill high-temperature area (Bjornsson, 1986). For instance, a resistivity map was obtained (Gunnarsson et al., 1992). Within the IGET project, Transient Electromagnetism surveys and 3D magneto-telluric profiles have been acquired over the area (Arnasson et al., 2008). Inversion of MT data reveals a low resistivity vertical cylindrical body below Olkelduhals at depths ranging 3-5 km, and spread as an elongated structure oriented NW-SE at greater depth. Figure 24 shows a superposition of the results of the two inversions. We observe a close match between a low resistivity anomaly and high P-wave velocity between 2 and 4 km depth. This joined anomaly is close to the inflation source location observed in 1995 (Feigl et al., 2000).

Future work will focus of the analysis of the source mechanism of the observed earthquakes and relate them to the fluid exploitation.

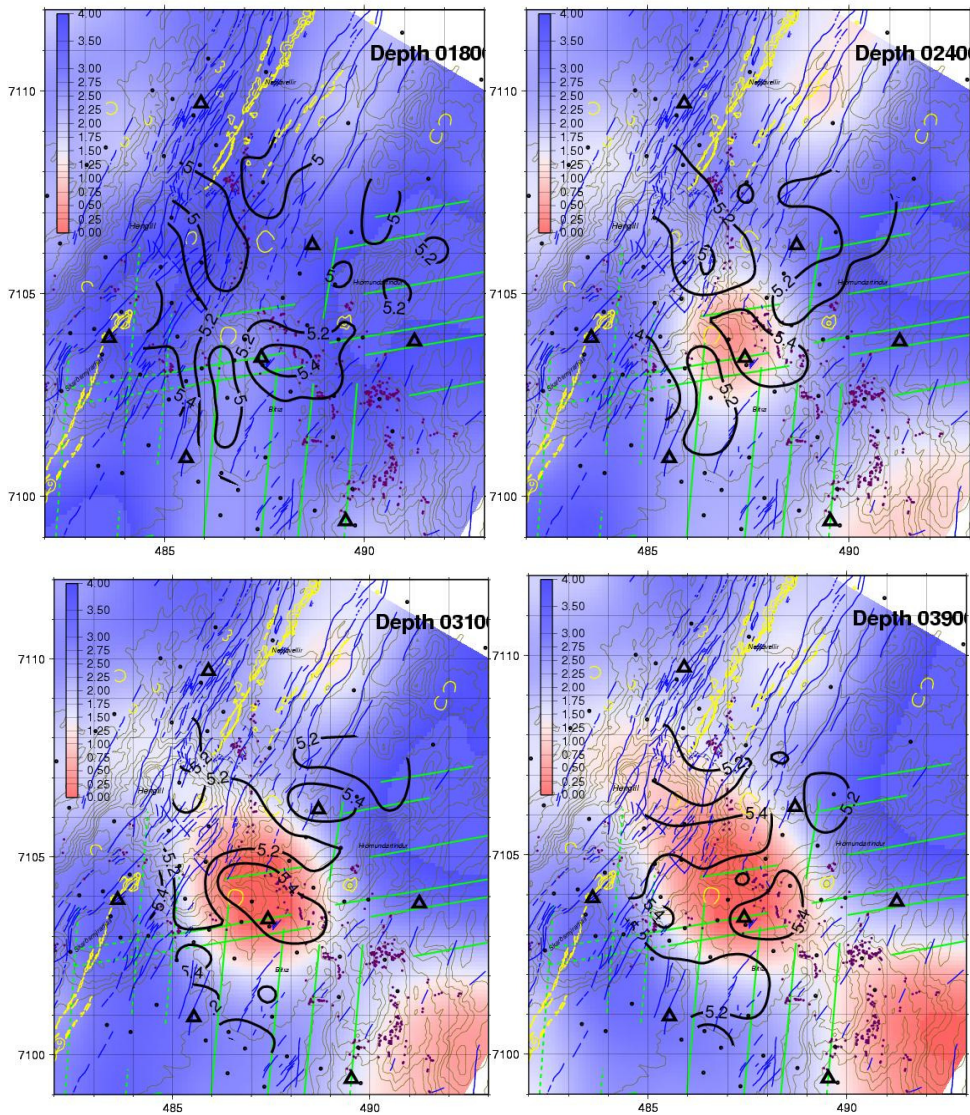


Figure 24 – Comparison between the resistivity model obtained from the inversion of TEM and magnetotelluric data (Arnasson et al., 2008) and the P-wave velocity model obtained from the tomography of broadband observations at Hengill geothermal system at different depths (left, top: 1800m; right, top: 2400 m; left, bottom: 3100 m; right, bottom: 3900 m).

Acknowledgements: Knutur Arnasson (ISOR) provided ISOR facilities for the field work. Summer students helped us in setting up stations: Egill Árni Guðnason, Gunnar S. Hilmarsson, Halldór Örvar Stefánsson; Jón Einar Jónsson; Sæmundur Ari Halldórsson; Þorbjörg Ágústsdóttir; Þórhildur Björnsdóttir.

6. References

- Agutsson K and P. Halldorsson, 2005. Seismic hazard in the Hengill area based on the SIL earthquake catalogue – First results. Report 05015, Vedurstofa Islands, Reyjavik, 41 p.
- Akaike, H. (1973). Information theory and an extension of the maximum likelihood principle. In Budapest Akademiai Kiado, pages 267-181. B. petrov and F. Csaki (Editors).
- Allen, R.V. (1982). Automatic phase pickers: their present use and future prospects. *Bull. Seismol. Soc. Am.*, 72:S225-242.
- Arnason K., H. Eysteinnsson and G. P. Hersir, 2008. Joint 1D inversion of TEM and MT data and 3D inversion of MT data in the Hengill area, SW Iceland, 2008. Geothermics, submitted.
- Barnea, J. (1972). United Nations approach and accomplishments in the field of geothermal resources development. *Geothermics*, 1:164-167.
- Benz, H.M., Chouet, B.A., B.Dawson, P., Lahr, J.C., Page, R.A., and Hole, J.A. (1996). Three-dimensional P and S wave velocity structure of Redoubt volcano, Alaska. *J. Geophys. Res.*, 101(B4):8111-8128.
- Bödvarsson G., 1961. Physical characteristics of natural heat ressources in Iceland. *Jökull*, 11, 29-38.
- Brenguier, F., Shapiro, N. M., Campillo, M., Nercessian, A., and Ferrazzini, V. (2007). 3-D surface wave tomography of the Piton de la Fournaise volcano using seismic noise correlations. *Geophys. Res. Lett.*, page L02305.
- Chaterjee, S., Pitt, A., and Iyer, H. (1985). VP/VS ratios in the Yellowstone National Park Region, Wyoming. *J. Volcanol. Geotherm. Res.*, 26:213-230.
- Chouet, B. (1996). New methods and future trends in seismological volcano monitoring., pages 23-97. Scarpa/Tilling, Springer-Verlag, Berlin Heidelberg.
- Dangel S. , M.E. Schaepman, E.P. Stoll, R. Carniel, O. Barzandji, E.D. Rode and J.M Singer, 2003. Phenomenology of tremor-like signals observed over hydrocarbon reservoirs. *J. Volcanol. Geotherm. Res.*, 128, 135-158.
- Eberhart-Phillips, D. (1986). Three-dimensional velocity structure in the northern California coast ranges from inversion of local earthquake arrival times. *Bull. Seismol. Soc. Am.*, 76:1025-1052.

- Eberhart-Phillips, D. (1990). Three-dimensional P and S velocity structure in the Coalinga region, California. *J. Geophys. Res.*, 95:15343-15363.
- Eberhart-Phillips, D. (1993). Local earthquake tomography: earthquake source region, pages 613-643. Eds Iyer, H.M and Hihara K. and Chapman & Hall, London.
- Eberhart-Phillips, D. and Michael, A.J. (1998). Seismo-tectonics of the Loma Prieta, California, region determined from three-dimensional VP, VP/VS, and seismicity. *J. Geotherm. Res.*, 103(B9):21099-21120.
- Ellworth, W.L., Eberhart-Phillips, D., and Kissling, E. (1991). A test of local earthquake tomography. *Seism. Res. Lett.*, 62:31.
- Ellworth, E. K.W., Eberhart-Phillips, D., and Kradolfer, U. (1994). Initial reference models in local earthquake tomography. *J. Geophys. Res.*, 99:19635-19646.
- Evans, J.R., Eberhart-Phillips, D., and Thurber, C.H. (1994). User's manual for SIMULPS12 for imaging VP and VP/VS: a derivative of the "thurber" tomographic inversion SIMUL3 for local earthquakes and explosions. USGS - Open-file report, 94-431:1-101.
- Evans, J.R., Foulger, G.R., Julian, B.~R., and Miller, A. (1996). Crustal shear-wave splitting from the local earthquakes in the Hengill triple junction, southwest Iceland. *Geophys. Res. Lett.*, 23(5):455--458.
- Feigl, K., J. Gasperi, F. Sigmundsson, and A. Rigo (2000), Crustal deformation near Hengill volcano, Iceland 1993–1998: Coupling between magmatic activity and faulting inferred from elastic modeling of satellite radar interferograms, *J. Geophys. Res.*, 105(B11), 25655-25670.
- Foulger, G.R. and Long, R. (1984). Anomalous focal mechanism solutions: evidence for tensile crack formation on an accretionary plate boundaries. *Nature*, 310:43-45.
- Foulger, G.R. (1988a). The Hengill triple junction, SW Iceland: 1. tectonic structure and the spatial and temporal distribution of local earthquakes. *J. Geophys. Res.*, 93:13493-13506.
- Foulger, G.R. (1988b). The Hengill triple junction, SW Iceland: 2. anomalous earthquake focal mechanisms and implications for process within the geothermal reservoir and at accretionary plate boundaries. *J. Geophys. Res.*, 93:13507-13523.
- Foulger, G.R., Long, R., P., E., and Björnsson, A. (1989). Implosive earthquakes at the active accretionary plate boundary in Iceland. *Nature*, 337:640-642.
- Foulger G. and D. Toomey (1989). Structure and evolution of the Hengill-Grensdalur Volcanic complex, Iceland: geology, geophysics and seismic tomography. *J. Geophys. Res.*, 94, B12, 17511-17522.

- Foulger, G.R. (1995). The Hengill geothermal area, Iceland: variation of temperature gradients deduced from the maximum depth of seismogenesis. *J. Volcanol. Geotherm. Res.* 65:119-133.
- Foulger, G.R., Miller, A., Julian, B., and Evans, J. (1995). Three-dimensional VP and VP/VS structure of the Hengill Triple Junction and geothermal area, Iceland, and the repeatability of tomographic inversion. *Geophys. Res. Lett.*, 22(10):1309-1312.
- Gunnarsson, A., Steingrímsson, B., Gunnlaugsson, E., Magnússon, J., and Maack, R. (1992). Nessjavellir geothermal co-generation power plant. *Geothermics*, 21(4):559-583.
- Haberland, C., Rietbrock, A., Lange, D., Bataille, K., and Hofmann, S. (2006). Interaction between fore-arc and oceanic plate at the south-central Chilean margin as seen in local seismic data. *Geophys. Res. Lett.*, 33:L23302.
- Henderson J.R., D.J. Barton and G.R. Foulger, 1999. Fractal clustering of induced seismicity in the Geysers geothermal area, California. *Geophys. J. Int.*, 139, 317-324.
- Humphreys, E. and Clayton, R.W. (1988). Adaptation of back projection tomography to seismic travel time problems. *J. Geophys. Res.*, 93:4731--4735.
- Iyer, H.M. and Hirahara, K. (1993). *Seismic Tomography: Theory and practice.* Chapman and Hall, London, UK.
- Jakobsdóttir S., 2008. Seismicity in Iceland, *Jökull*, 58, 75-100.
- Jousset P. and Jürgen Neuberg and S. Sturton, 2003. Modelling the time-dependent frequency content of low-frequency volcanic earthquakes. *J. Volcanol. and Geotherm. Res.*, 128, 201-223.
- Jousset P., S. Bès de Berc, H. Fabriol and B. Chouet, 2004. Monitoring and exploration of geothermal fields using broadband seismology: application to Bouillante, Guadeloupe, IAVCEI General Assembly, Pucon, Chile, 14th-19th, November, Symposium 8. 508b-pf-126.
- Jousset, P. (2006). *Sismologie large bande: méthodologie et applications: apport en géothermie haute enthalpie à Bouillante, Guadeloupe.* Rapport BRGM RP-54701-FR, page 119 pp.
- Jousset P. and B. François, 2006. Set-up of a broadband seismological network at Hengill geothermal field. BRGM report RP-54971-FR, 51 pp.
- Jousset P., K. Arnason, M. Weber, H. Fabriol, B. François, H. Stefansson and S. Jakobsdóttir, 2007. Preliminary observations of broad-band seismological records at Hengill geothermal system. ESC annual meeting, Reykjavik, September 2007.

- Jousset P., K. Arnason, M. Weber, H. Fabriol, B. François, H. Stefansson and S. Jakobsdottir, 2008a. Broad-band seismological observations at Hengill triple junction geothermal system. EGU meeting, Vienne 14-18 avril 2008.
- Jousset P., Arnason K., Bauer K., Fabriol H., François B., Haberland C., Jakobsdottir S., Stefansson H. and Weber M., 2008b. Broad-band seismological observations at geothermal systems: example of Hengill volcano, Iceland. IAVCEI meeting, Reykjavik, 18-22 August 2008.
- Jousset, P. and Chouet, B., 2008. Sustained long-period seismicity in hydrothermal systems: evidence for underground geyser activity at Bouillante, Guadeloupe. *Geophys. Res. Lett.*, submitted.
- Jousset, P., Haberland C., Bauer C. and Arnason K., 2008c. Detailed structure of the Hengill geothermal volcanic complex, Iceland inferred from 3-D tomography of high-dynamic broadband seismological data. *Geothermics*, submitted.
- Jousset, P., Weber, M., Arnason, K., and Fabriol, H., 2008d. Broadband seismology observations at geothermal Hengill volcanic complex, Iceland. *J. Volcanol. Geotherm. Res.*, in prep.
- Julian, B.R., Miller, A., and Foulger, G.R. (1997). Non-double couple earthquake mechanisms at the Hengill-Grensdalur volcanic complex. *Geophys. Res. Lett.*, 24(7):743-746.
- Kissling, E. (1988). Geotomography with local earthquake data. *Rev. Geophys.*, 26:659-698.
- Kissling E., W.L. Ellworth, D. Eberhart-Phillips and U. Kradolfer, 1994. Initial reference models in local earthquake tomography. *J. Geophys. Res.*, 99, 19635-19646.
- Koulakov, I., Bohm, M., Asch, G., Luehr, B.-G., A.Manzanares, Brotopuspito, K., Fauzi, P., Purbawinata, M.~A., Puspito, N., Ratdomopurbo, A., Kopp, H., Rabbel, W., and E.Shevkunova (2007). P and S velocity structure of the crust and the upper mantle beneath central Java from local tomography inversion. *J. Geophys. Res.*, 112(B08310).
- Kumagai H., B. Chouet and M. Nakano, 2002. Temporal evolution of a hydrothermal system in Kuratsu-Shirane Volcano, Japan, inferred from the complex frequencies of long-period events. *J. Geophys. Res.*, 107, B10, 2236.
- Legrand D., S. Kaneshima and H. Kawakatsu, 2000. Moment tensor analysis of near-field broadband waveforms observed at Aso Volcano, Japan. *J. Volcanol. Geotherm. Res.*, 101, 155-169.
- Leonard, M. and Kennett, B. (1999). Multi-component autoregressive techniques for the analysis of seismograms. *Phys. Earth. Planet. Interiors*, 113:247-264.

- Lokmer, I., Bean, C., Saccorotti, G., and Patanè, D. (2007). Moment-tensor inversion of lp events recorded on Etna in 2004 using constraints obtained from wave simulation tests. *Geophys. Res. Lett.*, 34(22):L22316.
- Maeda, N. (1985). A method for reading and checking phase times in auto-processing system of seismic wave data. *Zisin=Jishin*, 38:365-379.
- Michellini, A. (1993). Testing the reliability of VP/VS anomalies in travel time tomography. *Geophys. J. Int.*, 114:405-410.
- Miller, A., Julian, B., and Foulger, G.R. (1998). Three-dimensional seismic structure and moment tensors of non-double couple earthquakes at the Hengill-Grensdalur volcanic complex, Iceland. *Geophys. J. Int.*, 133:309-325.
- Neuberg J., R. Lockett, M. Ripepe and T. Braun, 1994. Highlights from a seismic broadband array on Stromboli volcano, *Geophys. Res. Lett.*, 21, 9, 749-752.
- Norris, A. N., 1985. A differential scheme for the effective moduli of composites. *Mech. of Mater.*, 4, 1-16.
- Pratt G., Changsoo Shin and G.J. Hicks, 1998. Gauss-Newton and full Newton methods in frequency-space seismic waveform inversion. *Geophys. J. Int.* 133, 341-362.
- Riedel C., T. Petersen, F. Theilen and S. Neben, 2003. High b -value in the leaky segment of the Tjörnes Fracture Zone north of Iceland: are they evidence for shallow magmatic heat sources? *Geophys. J. Int.*, 128, 15-29.
- Roeker, S.W. (1982). Velocity structure of the Pamir-Hindu Kush region: possible evidence of subducted crust. *J. Geophys. Res.*, 87:945-959.
- Saemundsson, K. (1995). Hengill, Jarðhiti, Ummyndun og Grunnvatn, 1:25000 (Hengill, Geothermal, Alteration and Groundwater}. Orkustofunun.
- Sens-Schönfelder, C., Korn, M., and Stefánsson, R. (2006). Joint interpretation of the size and time distributions of seismic activity around the Hengill triple junction (SW Iceland) between 1993 and 1996. *J. Seismol.* doi:10.1007/s10950-006-9011-5.
- Stefánsson, R., Bödvarsson, R., Slunga, R., Einarsson, P., Jakobsdóttir, S., Bungum, H., Gregersen, S., Havskov, J., Hjélme, J., and Korhonen, H. (1993). Earthquake prediction research in the South Iceland Seismic Zone and the SIL Project. *Bull. Seismol. Soc. Am.*, 83:696-716.
- Thurber, C.H. (1983). Earthquake locations and three-dimensional crustal structure in the Coyote Lake area, central California. *J. Geophys. Res.*, 88(B10):8226-8236.
- Thurber, C.H. (1986). Analysis methods for kinematic data from local earthquakes. *Rev. Geophys.*, 24:793-805.

- Thurber, C.H. (1993). Local earthquake tomography: velocities and VP/VS theory, pages 563--583. Eds Iyer, H.M and Hihara K. and Chapman and Hall, London.
- Toomey, D.R. and Foulger, G.R. (1989). Application of tomographic inversion to local earthquake data from the Hengill-Grendalur central volcano complex, Iceland. *Phys. Earth and Plan. Int.*, 94:17497-17510.
- Tryggvason, A., Rögnvaldsson, S.T., and Flovenz, O.G. (2002). Three-dimensional imaging of the P and S-wave velocity structure and earthquake locations beneath Southwest Iceland. *Geophys. J. Int.*, 151:848-866.
- Usher M. J., R.F. Burch and C. Guralp, 1979. Wide-band feedback seismometers. *Phys. Earth Planet. Inter.*, 18, 38-50.
- Wadati, K., 1933. On travel time of earthquake waves, Part II. *Geophys. Mag.*, 7: 101-111.
- Waldhauser, F. and Elsworth, W. (2000). A double-difference earthquake location algorithm: method and application to the Northern Hayward fault, California. *Bull. Seism. Soc. Am.* 90(6):1353-1368.
- Ward, P.L. (1972). Microearthquakes: prospecting tool and possible hazard in the development of geothermal resources. *Geothermics*, 1:3-12.
- Yao Z. S. and R. G. Roberts and A. Tryggvason, 1999. Calculating resolution and covariance matrices for seismic tomography with the LSQR method. *Geophys. J. Int.*, 138, 886-894.
- Zhang, H., Thurber, C., and Rowe, C. (2003). Automatic P-wave arrival detection and picking with multiscale wavelet analysis for single-component recordings. *Bull. Seismol. Soc. Am.*, 93(5):1904-1912.



Scientific and Technical Centre
Development planning and natural risks Division
3, avenue Claude-Guillemain - BP 36009
45060 Orléans Cedex 2 – France – Tel.: +33 (0)2 38 64 34 34